RSC Advances

REVIEW

View Article Online
View Journal | View Issue

Cite this: *RSC Adv.*, 2023, **13**, 17476

Bismuth tungstate Bi_2WO_6: a review on structural, photophysical and photocatalytic properties

Aicha Elaouni,[a] M. El Ouardi,[ab] A. BaQais,[c] M. Arab,[b] M. Saadi[a] and H. Ait Ahsaine *[a]

Received 26th March 2023
Accepted 2nd June 2023

DOI: 10.1039/d3ra01987j

rsc.li/rsc-advances

This review paper provides a comprehensive overview of the recent trends in bismuth tungstate (Bi_2WO_6) research, covering its structural, electrical, photoluminescent, and photocatalytic properties. The structural characteristics of bismuth tungstate are explored in detail, including its different allotropic crystal structures with respect to its isotypic materials. The electrical properties of bismuth tungstate, such as its conductivity and electron mobility, are also discussed, along with its photoluminescent properties. The photocatalytic activity of bismuth tungstate is a particular focus, with recent advances in doping and co-doping strategies with metals, rare earth and other elements summarized. The limitations and challenges of using bismuth tungstate as a photocatalyst are also examined, such as its low quantum efficiency and susceptibility to photodegradation. Finally, recommendations for future research directions are provided, including the need for further studies on the underlying mechanisms of photocatalytic activity, the development of more efficient and stable bismuth tungstate-based photocatalysts, and the exploration of new applications in fields such as water treatment and energy conversion.

1. Introduction

Bismuth tungstate (Bi_2WO_6), also known as BWO, is a highly sought-after material due to its numerous applications in the production of electronic components. This material is versatile and can be used for a range of purposes including capacitors, humidity detectors, optical sensors, and thermistors.[1–3]

This material belongs to the family of Aurivillius phases ($n = 1$) of the general formula $Bi_2A_{n-1}BnO_{3n+1}$ (with A = Ca, Sr, Ba, Pb, Bi, Na, K and B = Ti, Nb, Ta, Mo, W, Fe).[4] The structure consists of alternating fluorine-like $[Bi_2O_2]^{2+}$ ionic layers and $[WO_4]^{2-}$ ionic layers, linked together to form "n" perovskite-like units $A_{n-1}B_nO_{3n+1}$. Its photocatalytic properties under visible irradiation were discovered in 1999 for the production of dioxygen by oxidation of water[5] and then exploited from 2003, for the mineralization of organic molecules (chloroform and acetaldehyde) by Ye and his team.[6] Its photocatalytic activity has since been widely used to degrade a wide range of molecules, in gaseous or aqueous form, or even microorganisms under visible irradiation.[7,8] Bi_2WO_6 has indeed a suitable crystal and electronic structure for photocatalysis under visible light. The tungstate Bi_2WO_6 has orthorhombic symmetry, and its structure is composed of alternating Bi_2O_2 sheets and layers of WO_6 octahedra linked together by the vertices. This stacking of alternately charged (+) and (−) sheets creates an electric field parallel to the (001) plane of the sheets that promotes the mobility of photo-generated charges in the material and facilitates the adsorption of molecules on the surface.[9,10] Several other semiconductors have also been utilized as photocatalysts, including ZnO, CeO_2, ZrO_2, SnO_2, CdS, and ZnS. However, titanium dioxide (TiO_2) has emerged as a popular choice for environmental remediation due to its chemical stability, low cost, and strong oxidizing power, as documented in studies conducted by ref. 11–14. Nonetheless, TiO_2 has certain limitations, such as its high gap (E_g = 3.2 eV), which restricts UV radiation absorption to only 4% of the solar spectral band, or 387.5 nm, as observed in studies by ref. 4, 15 and 16.

Since its initial study by Knight,[17] Bi_2WO_6 has garnered significant attention owing to its exceptional physical and chemical characteristics, including ferroelectricity, piezoelectricity, catalytic properties, and nonlinear dielectric susceptibility, as highlighted in research conducted by ref. 17 and 18. With a gap of 2.8 eV, Bi_2WO_6 can absorb longer wavelengths, making it ideal for solar-related applications. Despite ongoing research into Bi_2WO_6 and its derivatives, the field remains largely underdeveloped.[10]

It is noteworthy that a series of review articles have been recently published on the photocatalytic performance of Bi_2WO_6 and its application in environmental remediation. For example, in 2019, Yi and his team.[19], described the latest fabrication approaches for Bi_2WO_6 and even discussed the

[a]*Laboratoire de Chimie Appliquée des Matériaux, Centre des Sciences des Matériaux, Faculty of Sciences, Mohammed V University in Rabat, Morocco. E-mail: h.aitahsaine@um5r.ac.ma*

[b]*Université de Toulon, AMU, CNRS, IM2NP, CS 60584, Toulon Cedex 9, F-83041, France*

[c]*Department of Chemistry, College of Science, Princess Nourah Bint Abdulrahman University, P. O. Box 84428, Riyadh 11671, Saudi Arabia*

mechanism of the various morphologies of Bi_2WO_6. It was interesting to note that the photocatalytic activities of three bismuth-based photo-catalysts (Bi_2WO_6, Bi_2MoO_6 and $BiVO_4$) were also assessed in a review by Liu *et al.*[20] In the same context chen *et al.*[21], reviewed the fundamental photocatalytic principles of BWO as well as material modification approaches to enhance the photocatalytic capabilities of BWO, comprising atomic modulation, morphology control and composite manufacturing. This current review reports the advances and the recent applications, electrical and photoluminescent properties of BWO materials as well as the photocatalytic properties of bare and doped BWO photocatalysts.

2. Synthesis and characteristics of Bi_2WO_6 photocatalyst

Bi_2WO_6 is categorized as a layered perovskite-type oxide compound, consisting of bismuth (Bi), tungsten (W), and oxygen (O). Its distinctive structural and physicochemical properties have generated substantial interest. The dimensional morphology of Bi_2WO_6 is closely linked to its physical structure and shape.[22] Understanding the influence of various synthesis methods and morphologies on Bi_2WO_6 is crucial, as they have a significant impact on its characterization and properties. Therefore, gaining insight into how different synthesis methods and conditions can yield diverse morphologies of Bi_2WO_6 is vital for a comprehensive understanding of its characterization. It is worth noting that each synthesis method possesses its own set of advantages and disadvantages. Presented below are some commonly employed synthesis methods.

2.1. Solid-state synthesis

This method utilizes easily accessible precursors and is characterized by its simplicity and cost-effectiveness. It involves the direct solid-state reaction between bismuth oxide (Bi_2O_3) and tungsten oxide (WO_3) at elevated temperatures.[23] However, the use of high temperatures can influence the crystal structure, potentially leading to particle aggregation and the formation of larger crystals. This, in turn, can have implications for the material's optical, electrical, and catalytic properties, as well as its potential applications.[24]

2.2. Hydrothermal/solvothermal method

This process utilizes either an autoclave or a sealed container to facilitate the reaction between bismuth and tungsten precursors in a water-based solution at high pressure and temperature. By employing this technique, precise control over the particle size, shape, and crystal structure is achieved, resulting in enhanced properties and the formation of Bi_2WO_6.[25,26] However, it should be noted that this method requires specialized equipment and longer reaction times when compared to alternative approaches. The solvothermal method,[27] which is similar to the hydrothermal technique, offers another option. It allows for better regulation of the particle size, shape, and crystal structure of Bi_2WO_6 through the manipulation of factors such as reaction temperature, duration, precursor concentration, and pH. Nonetheless, the solvothermal method also calls for specialized equipment and longer reaction durations.

2.3. Sol–gel method

In this technique, a colloidal suspension (sol) is formed, which later undergoes gelation to create a solid network. The sol–gel method allows for effective management of composition, purity, and homogeneity. It also offers the possibility of incorporating dopants and customizing properties. However, it is important to note that this process is relatively intricate, involving multiple steps. Longer processing times are necessary for both gel formation and subsequent thermal treatment.[28]

2.4. Microwave-assisted

Synthesis involves utilizing microwave irradiation to heat a reaction mixture that contains bismuth and tungsten precursors.[29] This approach provides several advantages, such as rapid heating and shorter reaction times. Additionally, it results in enhanced crystallinity and improved phase purity when compared to conventional methods. However, there are some drawbacks to consider. The scalability of this technique for large-scale production is limited. It is crucial to optimize the reaction parameters carefully to prevent overheating or the formation of localized hotspots.

The selection of a synthesis method depends on specific requirements, desired properties, and available resources. Factors such as cost, scalability, purity, control over morphology, and crystallinity are typically considered by researchers to determine the most suitable approach. In order to enhance photocatalytic activity, various structures of Bi_2WO_6 photocatalysts, including three-dimensional, two-dimensional, one-dimensional, and zero-dimensional, have been successfully synthesized using these methods. These photocatalysts have demonstrated impressive effectiveness across a wide range of applications. Among different metal oxide semiconductors responsive to visible light, bismuth-based catalysts, particularly bismuth tungstate (Bi_2WO_6), have shown significant potential in energy production and environmental treatment. Bi_2WO_6 has gained substantial attention for its efficient removal of organic pollutants from wastewater through photocatalysis. With a suitable band gap energy of 2.8 eV, Bi_2WO_6 effectively absorbs photons in the visible light region. While efforts have been made to improve the photocatalytic performance of semiconductors by incorporating rare-earth metals, Bi_2WO_6 benefits from its inherent properties, reducing the need for complex methodologies. Table 1 provides a summary comparing Bi_2WO_6 with common Bismuth-based catalysts and recently employed photocatalysts. While other bismuth-based catalysts may have advantages in specific applications, Bi_2WO_6's favorable band gap, visible light absorption, high performance, inherent properties, and broad applicability make it a preferred choice for many researchers and practitioners in the field. Additionally, the choice of BWO is explained by its simple synthesis methods with different morphologies and shapes, easiness to remediate its drawbacks of rapid recombination of charge

Table 1 Comparing Bi_2WO_6 with common bismuth-based catalysts, their advantages, and disadvantages

Bismuth-based catalysts	Materials	Advantages	Disadvantages	Environmental application	Ref.
Bismuth vanadate	$BiVO_4$	Low band gap, excellent dispersibility, non-toxic nature, corrosion resistance, and exceptional photocatalytic performance in degrading organic pollutants under visible light	Overall photocatalytic activity is limited by the relatively low mobility of charge carriers it exhibits	Water splitting, photocatalytic degradation of pollutants, solar fuel production, antibacterial applications, air purification	30 and 31
Bismuth molybdate	Bi_2MoO_6	Being a visible light-responsive catalyst used in photocatalytic applications such as water purification and pollutant degradation with a good photocatalytic efficiency and stability	Its main limitation is its relatively wide bandgap, which limits its absorption of visible light and reduces overall efficiency	Photocatalysis, water treatment, air purification, solar fuel, production, energy storage	32
Bismuth-based perovskites	$BiFeO_3$ $BiMnO_3$	Exhibit exceptional stability and offer a broad spectrum of multifunctional properties. Including water splitting, CO_2 reduction, and catalytic energy storage	The synthesis of bismuth-based perovskites presents challenges, and their overall efficiency can be constrained by defects and surface reactivity, which have an impact on their performance	Photocatalysis, water splitting, solar cells Wastewater treatment, gas sensors, energy storage	33
Bismuth-based zeolites	Bismuth-containing ZSM-5 zeolite Bismuth-containing beta zeolite Bismuth-exchanged Y zeolite Bismuth-containing MFI zeolite	In the processes of NO_x reduction and hydrocarbon conversion, these catalysts demonstrate notable activity and exhibit a high level of selectivity	The synthesis process of these catalysts can involve complexity, and various factors such as metal loading, acidity, and reaction conditions can influence their catalytic performance	Catalytic applications, adsorption and separation, environmental sensing, energy storage and conversion	34
Bismuth tungstate	Bi_2WO_6	Suitable band gap exhibits responsiveness to visible light, demonstrates exceptional effectiveness in achieving photocatalytic efficacy, and maintains good chemical and thermal stability	Bi_2WO_6 exhibits a tendency towards rapid charge carrier recombination, which can detrimentally impact its overall photocatalytic efficiency. Achieving efficient charge separation and effectively suppressing recombination pathways are pivotal factors in enhancing the catalytic performance of Bi_2WO_6	Photocatalysis, antibacterial applications, self-cleaning surfaces, water splitting for hydrogen production, environmental sensors	34

carrier using, cocatalysts, different morphologies and shapes, doping, co-doping *etc.*

3. Structural properties of Bi_2WO_6 and its isotypic materials

Both Bi_2WO_6 and Bi_2MoO_6 compounds are known to exist in three polymorphic phases that are temperature-dependent. At room temperature, both compounds adopt an orthorhombic structure, known as the L phase with space group $P2_1ab$, and exhibit ferroelectricity. The structure consists of alternating $[Bi_2O_2]^{2+}$ fluorine layers and $[MO_4]^{2-}$ layers, which contain octahedral units, as depicted in Fig. 1a. Bi_2WO_6 exhibits a medium-temperature orthorhombic form (phase I) that has a higher symmetry with space group $B2cb$, but the connectivity is similar to the low-temperature orthorhombic phase (L). The high-temperature monoclinic form (phase H) of Bi_2WO_6 (Fig. 1b) still retains its layered nature, but the $[MO_4]^{2-}$ moieties now contain octahedral-bonded side chains, as reported in studies by ref. 35.

In the case of Bi_2MoO_6, the three polymorphisms are generally referred to as γ, γ″ and γ′ or γ(L), γ(I) and γ(H) for the low, medium and high temperature phase respectively.[36,37] In the case of Bi_2WO_6, the (L) and (I) phases are closely related

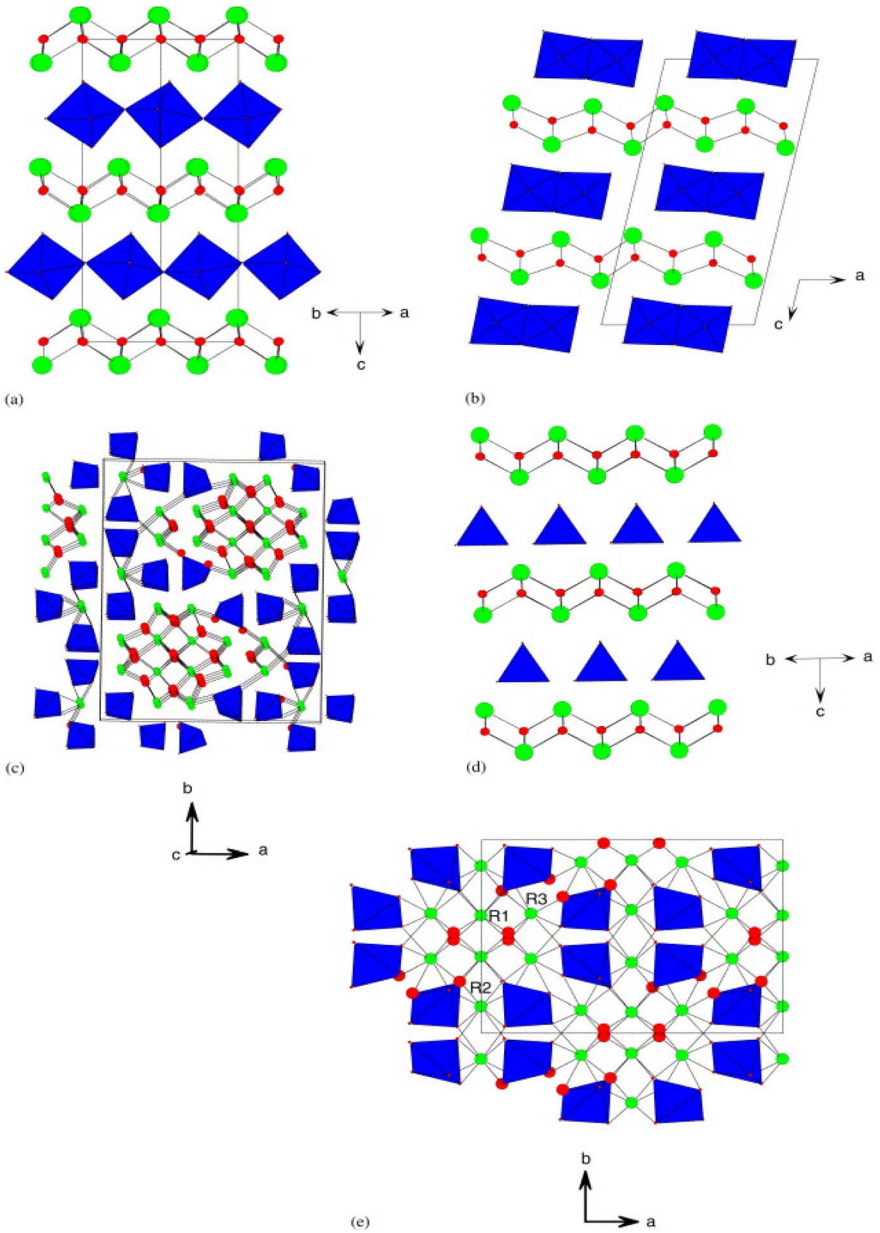

Fig. 1 (a) The structure of the L-Bi_2WO_6 phase, space group $P2_1ab$; (b) the structure of the H-Bi_2WO_6 phase, space group $A2/m$; (c) the structure of γ(H)-Bi_2MoO_6, space group $P2_1/c$; (d) the structure of La_2MoO_6, space group $I4_1/a$; and (e) the structure α-R_2MoO_6, space group $C2/c$ (reproduced with permission from ref. 35 with permission from Wiley-VCH, Copyright 2006).

to orthorhombic Aurivillius-like structures, but the monoclinic γ (H) phase at high temperature is very complex. Fig. 1c depicts this structure, which has been described as "columnar" and contains isolated $[MO_4]^{2-}$ tetrahedral units.[38,39] Bismuth tungstate Bi_2WO_6 has three structural transitions: the first occurs at 660 °C with a space group change from $P2_1ab$ to $B2cb$; the second paraelectric–ferroelectric transition occurs at about 930 °C and finally an orthorhombic–monoclinic phase transition at 960 °C with the space group changing to $A2/m$.[35,40,41]

The $Bi_{2-x}TR_xMO_6$ solid solution series (with M = W or Mo and RE = rare earth) exhibits several structure types at the opposite end of the series ($x = 2$), depending on the nature of elements RE and M. For instance, La_2MoO_6 compound has a quadratic structure that is closely related to Aurivillius phases. It comprises fluorine-like layers $[La_2O_2]^{2+}$ and tetrahedral layers $[MoO_4]^{2-}$ as illustrated in Fig. 1d.[42] On the other hand, Pr_2MoO_6 and Nd_2MoO_6 adopt a monoclinic (H) γ-TR_2MoO_6 structure, while Ce_2MoO_6 adopts a pseudoclinic (β-polymorph) structure, whose details remain unknown. In the case of TR lanthanides with low ionic radii, the structure observed is of the α-TR_2MoO_6 type ($C2/c$ monoclinic), which exhibits a complex superstructure related to fluorine layers containing isolated $[MoO]_5$ polyhedra, as shown in Fig. 1e.[43,44] Tyulin and Efremov[45] reported seven polymorphic forms, including quadratic I (observed in the case of lanthanum) and monoclinic II (in the cases of TR = Ce–Ho, Y), which are identical to α-TR_2MoO_6. The remaining forms (III–VII) have completely different structures.

Numerous investigations have been carried out on $Bi_{2-x}TR_xMO_6$ solid solutions. In the case of M = W, Watanabe discovered monoclinic phases of $P2/c$ symmetry for all lanthanides over a range of compositions from 0.3 to 1.3.[46] Meanwhile,[47] recently demonstrated that this phase corresponds to H-Bi_2WO_6 ($A2/m$) and conducted a detailed structural analysis of $Bi_{0.7}Yb_{1.3}WO_6$ using neutron diffraction.[48] As for molybdates, the $Bi_{2-x}TR_xMoO_6$ solid solution also exhibits an H-Bi_2WO_6-like phase,[48] as seen in the case of the compound $Bi_{2-x}Nd_xMoO_6$ in the compositional range $0.4 < x < 0.7$.

According to Taoufyq and coworkers[49] The non-centrosymmetric space group $Pca2_1$, which had been previously suggested for this phase, was confirmed by both the Rietveld analysis and electron diffraction. Furthermore, they have delivered the first direct imaging of structural layers with the two types of sandwiches of $Bi_2O_2^{2+}$ (Bi–O–Bi layers) and WO_4^{2-} (O–W–O layers) chemical entities. Generally, these pure phases can be obtained by solid-state synthesis, using careful selection of sintering temperature and time, cooling rate and even the rate of alkali metal used.[47]

3.1. Electrical properties

These materials present multiple interesting properties including their piezoelectricity, their ferroelectricity and their non-linear dielectric susceptibility.[35,36,50,51]

Piezoelectricity is a property possessed by certain crystalline phases that become electrically polarized under the action of a mechanical stress, and conversely deform when an electric field is applied to them. This property is used in acoustic, shock and vibration wave sensors.[52] Ferroelectricity refers to a material's ability to exhibit an electrical polarization in its spontaneous state, which can be reversed by an external electric field. Bi_2WO_6 displays complex conduction properties. At temperatures below 700 °C and oxygen partial pressures of 1 to 10–1 atm, Mączka *et al.* found that Bi_2WO_6's conductivity is mostly ionic, but for pressure values below 10–1 atm, it is mostly electronic.[53]

In a separate study, Salkus *et al.*[54] investigated the electrical impedance properties of Bi_2WO_6 pellets and discovered that electronic conductivity is highly dependent on oxygen activity (Fig. 2): lowering oxygen activity results in an increase in n-type conduction, while high oxygen activity yields p-type conduction. This behavior is typical of oxygen ionic conductors, in which redox reactions occur as a function of oxygen partial pressure. Both n- and p-type electronic conductivities begin to saturate at the extremes of oxygen activity. Generally, oxygen vacancies associated with negative electronic charges in the conduction band are the majority of defects in the n conduction domain, whereas cationic vacancies associated with positively charged holes in the valence band are the majority of defects in the p conduction domain.

The impedance spectra of Bi_2WO_6 were found to exhibit two distinct regions of dispersion, as noted by the authors. To simulate these spectra, they used an equivalent circuit consisting of two circuits. At high frequencies, the first circuit consisted of a resistor and a constant-phase element in parallel (Rb//CPEb), which described the movement of charge carriers within the ceramic bulk. The second circuit was composed of a resistor and a constant-phase element in parallel (Rgb-CPEgb), which described the movement of charge carriers through the grain boundaries of the ceramic (Fig. 3b). The authors also observed an ion blocking effect at the solid–electrode interface at 800 K. The conductivities σ_b and σ_{gb} were then calculated (Fig. 3b), and their activation energies were found to be 0.92 and 1.44 eV, respectively.

Toufyq *et al.*,[49] have investigated the electrical properties under air and argon. Authors have used electrical impedance spectrometry (EIS) and direct current (DC) analyses were used to determine the electrical properties of Bi_2WO_6 compacted pellets systems between 350 and 700 °C, under air and argon conditions. The DC analyses revealed that the conduction observed from EIS analyses was primarily ionic in nature within this temperature range, with a minor electronic contribution. Electrical changes were observed above the transition temperature of 660 °C, under both air and argon atmospheres (Fig. 4). The significant increase in conductivity observed under argon is explained by the formation of additional oxygen vacancies, coupled with electron conduction.

3.2. Photoluminescence properties

Luminescent materials are used for the detection of low or high energy radiation, UV, X-rays or γ-rays, by converting them into UV, visible, or infrared emission, with wavelengths

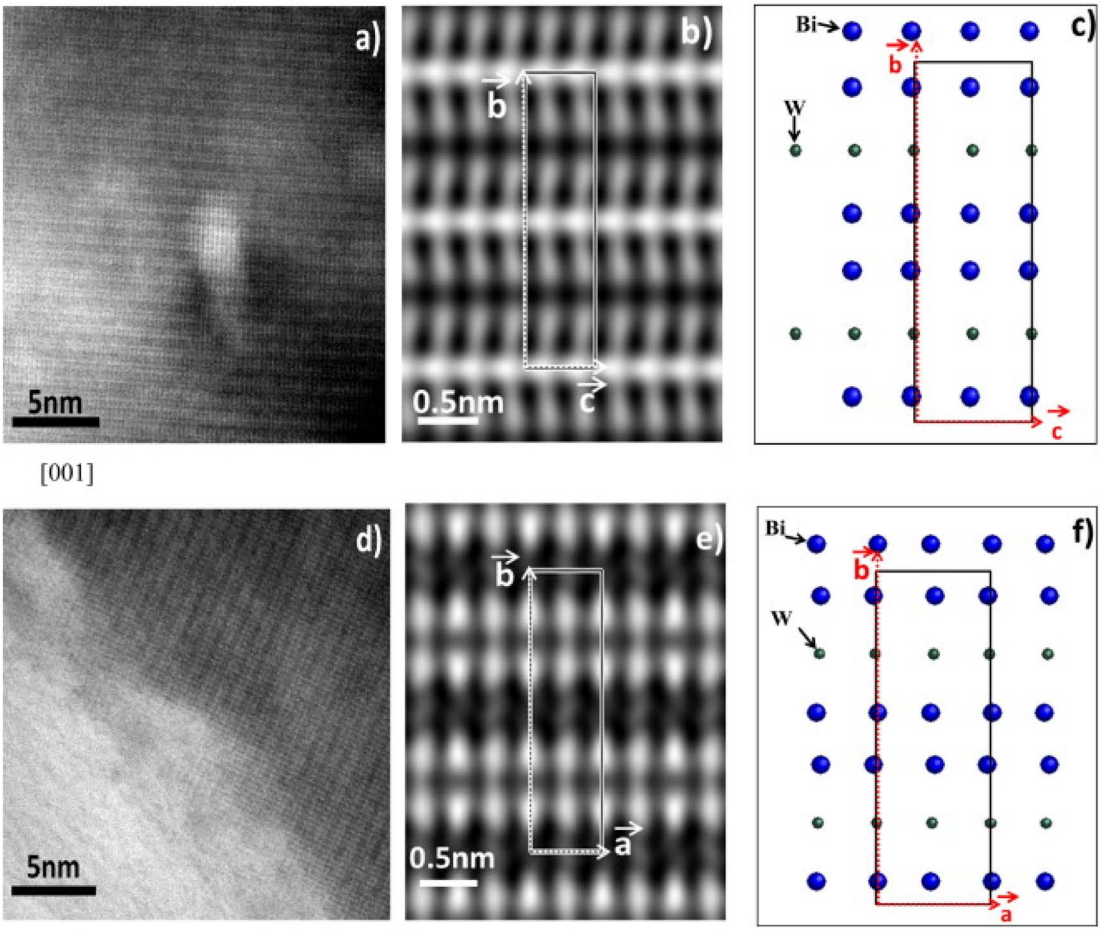

Fig. 2 High resolution TEM images of Bi_2WO_6 (reproduced from ref. 49 with permission from Elsevier, Copyright 2013).

corresponding to the sensitivity domains of the different photodetectors (photomultiplier, photodiode, photographic film, CCD camera, amorphous silicon…).[55]

The process of luminescence is extremely complex. We can describe the phenomenon of luminescence in three main steps: the absorption of a photon of suitable energy, then the creation of electron–holes and finally the recombination of the pairs with emission of photons (Fig. 4). In the case of a semiconductor the excitation of the electrons of the valence band is obtained from photons of energy higher than the gap in general.

In the case of doping, the electrons and holes thus created relax and can transfer their energy towards the luminescent center which can be a dopant, a defect or a molecular grouping and finally the last stage is the luminescence of the activator center.

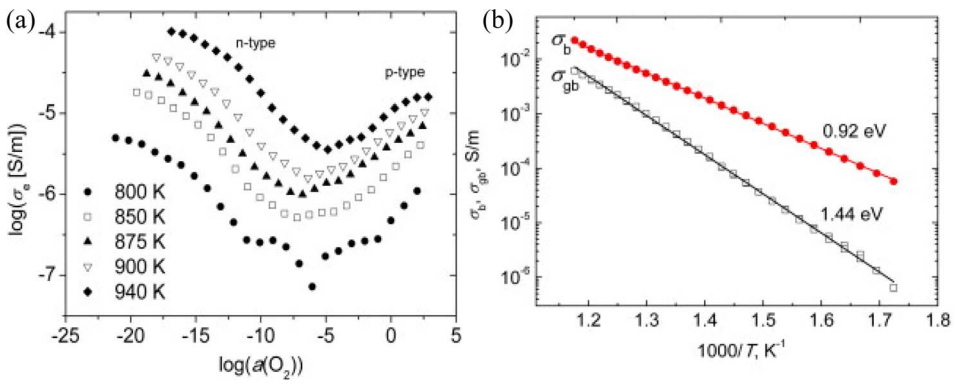

Fig. 3 (a) The variation of electronic conductivities as a function of O_2 activity at different temperatures in BWO, (b) variation of σ_b and σ_{gb} conductivities as a function of BWO temperature (reproduced from ref. 54 with permission from Elsevier, Copyright 2015).

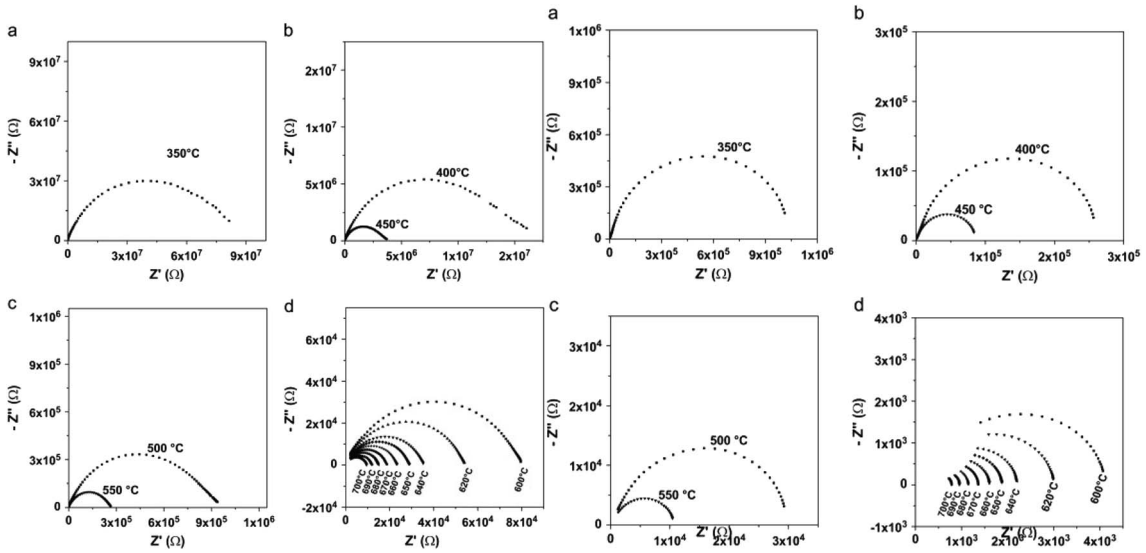

Fig. 4 (Left) Typical Nyquist representations for compacted pellet of Bi_2WO_6, as a function of temperature, under air; (a) $T = 350$ °C, (b) 400 °C $\leq T \leq$ 450 °C, (c) 500 °C $\leq T \leq$ 550 °C, (d) 600 °C $\leq T \leq$ 700 °C. (Right) Typical Nyquist representations for compacted pellet of Bi_2WO_6, as a function of temperature, under argon flow; (a) $T = 350$ °C, (b) 400 °C $\leq T \leq$ 450 °C, (c) 500 °C $\leq T \leq$ 550 °C, (d) 600 °C $\leq T \leq$ 700 °C. (reproduced from ref. 49 with permission from Elsevier, Copyright 2013).

3.3. Luminescent properties of pure and substituted BWO phase

In recent studies, the luminescent properties of scheelite and wolframite tungstates have been explained in two ways. Firstly, it has been suggested that the luminescence arises from electronic charge transfer occurring within complex $(WO_4)^{2-}$ oxyanions or from luminescent defects in WO_3.[56] Secondly, Van Oosterhout *et al.*[57] used a molecular orbital model to demonstrate that the excited state corresponds to an electronic transition from the 2p oxygen orbital (O 2p) to the 5d tungsten orbital (W 5d) with t_{2g} symmetry. According to this model, the emission spectra involve transitions from the double ^3T_1u levels (triplet states) to the inner $^1Ag_1$ level (singlet state). Other researchers[58–61] have put forth similar interpretations. Some of them have described the fundamental emission in structures resembling scheelite as transitions from two triplet states ($^3T_1$ and $^3T_2$) to the ground state 1A1, involving charge transfer in oxyanions $(WO_4)^{2-}$. Similarly, in wolframite structures, they suggest transitions from two triplet states (^3T_1u and ^3T_2u) to the ground state $^1A_{1g}$, again involving charge transfer in oxyanions $(WO_6)^{6-}$. Additionally, in the case of octahedral $(WO_6)^{6-}$ oxyanions, two extra transitions with lower energies have been taken into account. The emission and absorbance for both structures are depicted in Fig. 5, with the blue and red arrows indicating the respective processes. The dotted arrows represent forbidden transitions. To recap, the ground state $^1A_1$ can be visualized as the configuration where the oxygen's O 2p orbitals are fully occupied, while the tungsten's W 5d antibonding orbitals remain empty, resulting in a total spin of $S = 0$. The spectroscopic terms ^3T or ^1T correspond to the excited state, where an electron from oxygen moves to one of the W 5d levels of tungsten, leaving an unpaired electron on oxygen. Depending on the spin number, two distinct excited states with different energies and characteristics can be identified: the unstable singlet state (1T: total spin $S = 0$) and the triplet state (^3T: total spin $S = 3$). In the case of compounds containing bismuth, photoluminescence signals under UV excitation have been attributed to internal bismuth transitions.[62] The authors have employed theoretical calculations to explain emissions occurring within the range of 300 to 600 nm in the UV-visible spectrum, as well as emissions in the near infrared (NIR)

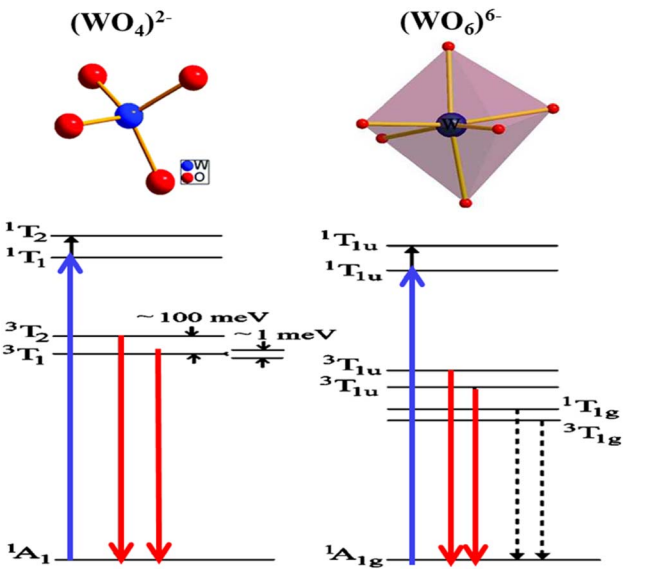

Fig. 5 The energy levels of the photoluminescence process in scheelite $(WO_4)^{2-}$ and wolframite $(WO_6)^{6-}$ structures. This figure was modified for understanding purpose and (reproduced from ref. 58 with permission from AIP Publishing, Copyright 2005).

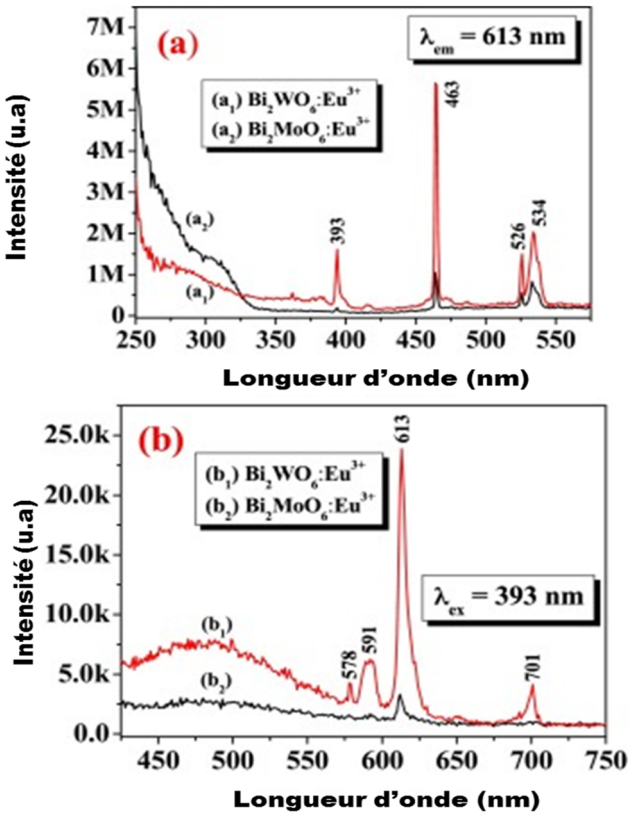

Fig. 6 The emission of bismuth tungstate doped by europium according to the authors (reproduced from ref. 64 with permission from ASP, Copyright 2010).

region, specifically between 800 nm and 1500 nm or beyond. PIR emissions have frequently been observed in various doped bismuth materials, including glasses.[63] These NIR emissions rely on the excitation energies and the characteristics of the matrix material itself. The origins of these emissions are still a subject of extensive discussion in the literature. It is hypothesized that these emissions could be produced by bismuth species such as Bi^{2+}, Bi^{+}, or by more complex bismuth-based molecules functioning as luminescent defects.

Few studies have been performed on the luminescence of substituted bismuth tungstates under UV or high energy radiation (X-rays, γ-rays). Recently, some studies have been developed to amplify the emission in the red by doping the BWO phase with Eu^{3+} europium ions (Fig. 6): the energy level of these ions is placed in the band gap, which favors the charge transfers between the energy levels of the BWO bismuth tungstate and the europium levels (4f–4f or 4f–5d level).[64,65]

The luminescent properties of Bi_2WO_6 are primarily attributed to the radiative decay of the anionic complex $[WO_4]^2$. This has been supported by studies on MWO_4 compounds (where M = Pb, Ca and Zr) with a quadratic scheelite structure, which have shown that the nature of the M^{2+} cation does not affect the luminescence spectrum, which is solely determined by the $[WO_4]^2$ complex.[66] In orthorhombic bismuth tungstate Bi_2WO_6, the luminescence is also determined by the $[WO_4]^2$ complex.[67] Bordun *et al.*[68] have confirmed these findings in their investigations on BWO and $PbWO_4$ thin films, which showed that the luminescence bands were related to the $[WO_4]^{2-}$ groups, even with substitutions or changes in crystal field symmetry. They also observed a strong electron–photon interaction, indicating the local character of the electronic excitations undergoing radiative decomposition. Based on research by ref. 48 and 66, the main luminescent bands of $PbWO_4$ and Bi_2WO_6 are due to self-localized Frenkel excitons, which describe the excited state of the $[WO_4]^2$ complex, with respective maxima at 2.8 eV and 2.93 eV.

To conclude, in bismuth tungstate BWO, luminescent bands are observed due to electronic transitions or charge transfers within the $[WO_4]^2$ complex. Previous works by ref. 69 and 70 interpret this emission as self-localized molecular excitons. Molecular orbital calculations for the $[WO_4]^{2-}$ complex of T_d symmetry reveal that the ground state $^1A_1$ has a t_{61} electronic configuration, and the excited states are $^1T_2 > {}^1T_1 > {}^3T_2 > {}^3T_1$, in decreasing order of energy. The allowed transitions from $^1A_1$ to $^1T_2$ and $^1T_1$ are considered the fundamental absorption limit, while the lower triplets $^3T_2$ and $^3T_1$ are responsible for radiative transitions. This finding is supported by previous studies by ref. 69, 71 and 72.

The spectral position and structure of the luminescent band are significantly affected by the coordination environment of the emitting center.[72] Monoclinic structures exhibit significant differences in luminescence properties compared to scheelite tungstates due to changes in tungsten environment and crystallographic data, particularly W–O distances.[72] Von Oosterhout's previous calculations,[72] based on a molecular orbital model for the $[WO_6]^{6-}$ octahedron, indicated that the highest state occupied by the T_{1g} symmetry is associated with the 2p orbital of oxygen and the excited state consists of an electron occupying the 5d orbital of tungsten with t_{2g} symmetry. As per the allowed transitions $^1A_{g1} \Rightarrow {}^1T_{1u}$, it is established that the absorption by the $[WO_6]^{6-}$ complex is attributed to these transitions (Fig. 5). Therefore, the most likely scenario for emission involves transitions from two $^3T_{1u}$ levels to the fundamental $^1A_{g1}$ energy level. Ait ahsaine *et al.*,[73] have studied the photoluminescence properties of different substituted BWO materials with lutetium (Fig. 7). Authors have found that the formation of the monoclinic structure induced by the substitution of bismuth with lutetium is closely linked to the photoluminescence observed under monochromatic UV excitation. The resulting emission can be classified into two types. The first is the conventional emission of WO_6^{6-} tungstate groups, which has two components attributed to charge transfers "W 5d O 2p" when octahedral coordination occurs. The second is a specific emission observed in the near-infrared region at 1.25 eV and is strongly correlated with the presence of lutetium. However, the exact origin of this emission remains uncertain. According to previous research on tungstates, it may result from defect centers originating from oxygen vacancies or defects in bismuth species with different valences or molecular clustering.

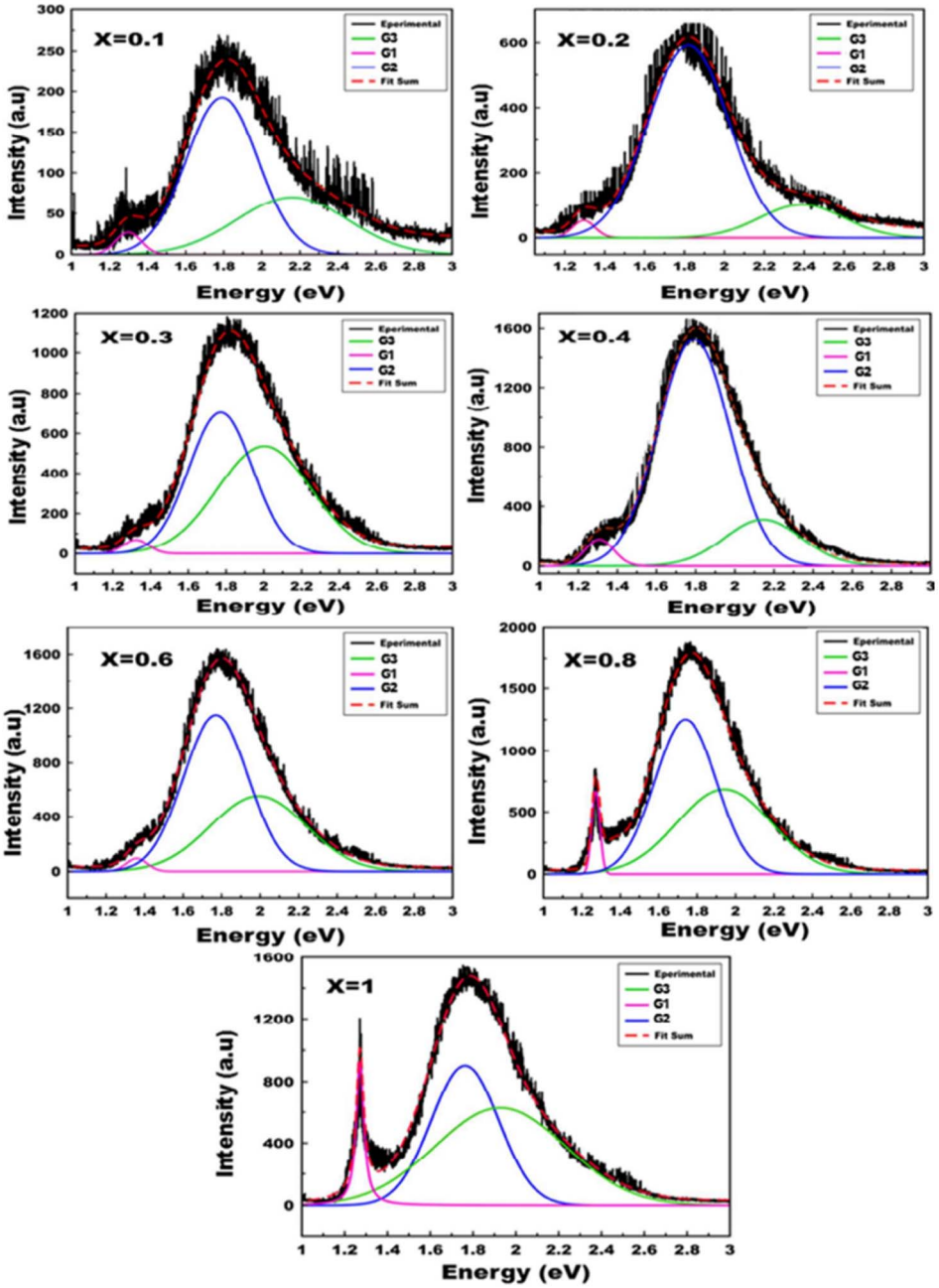

Fig. 7 Photoluminescence spectra of the $Bi_{2-x}Lu_xWO_6$ materials (reproduced from ref. 73 with permission from Royal Society of Chemistry, Copyright 2015).

4. Photocatalytic properties

Photocatalysis involves using UV or visible light to activate a semiconductor material, which then promotes redox reactions that degrade organic molecules in an aqueous medium.[74–77] The semiconductor's electronic structure consists of a valence band and a conduction band separated by a band gap. Upon irradiation with photons having energy greater than or equal to the band gap, electrons move from the valence band to the conduction band, generating electronic holes. The electron–hole pairs created in the photocatalyst may recombine or, if their lifetime is long enough, migrate to the surface of the photocatalyst and contribute to the photocatalytic reaction. Surface charge carriers can also be trapped before recombination or release. Recombination is the main limiting factor in photocatalysis because it prevents the use of surface charge carriers for catalytic oxidation reactions.[76,78]

4.1. The relationship between structure and photo-catalysis capacity of BWO photocatalyst

Bi_2WO_6, as one of the most common Aurivillius oxides, possesses an orthorhombic structure composed of $[Bi_2O_2]^{2+}$

layers connected to corner-shared $[WO_4]^{2-}$ layers. The arrangement and bonding within these layers affects the characteristics and performance of the Bi_2WO_6 as a photocatalyst.[79,80] The layered structure of BWO offers a wide surface area, allowing the provision of active sites for adsorption and reaction with target species. In addition, the unique sandwich architecture of BWO enables the induction of a built-in electric field between the layers, favoring the separation of the photogenerated holes and electrons.[21] In this context, Density Functional Theory (DFT) calculations may be used to examine the contribution of orbitals to the CB and VB. It is well known that the VB of BWO is formed by the hybrid orbitals of O 2p and Bi 6s, the CB of BWO is composed of W 5d orbitals.[81] On that basis, the band gap of BWO is usually between 2.6 and 2.9 eV, according to the position of VB and CB, making it a visible light sensitive photo-catalyst.[21] In the other hand, defects, like oxygen vacancies are commonly present in BWO photo-catalyst and can act as active sites for catalytic reactions. Recently, Liu *et al.*[82] demonstrated that with a high concentration of oxygen vacancies in Bi_2WO_6 surface, a photo-degradation of 100% of levofloxacin was achieved, they revealed that oxygen vacancies can not only speed up the separation of photo-generated charges, but can also activate O_2 molecules to form superoxide radical species.[82] In a related study, Yang and his team[83] demonstrated that the marked enhancement of photocatalytic performance in the decomposition of phenol and dyes may be ascribed to the synergistic impact of the oxygen deficiency-induced band shifts.[83] In addition to oxygen vacancies, the crystallinity and exposed crystal facets of BWO can have a major impact on its photocatalytic performance.[21] Various crystal facets may have different reactivity and surface characteristics, influencing the adsorption and reaction kinetics of desired molecules.[84] Facets with greater surface energy generally exhibit more exposed reactive sites, promoting the adsorption of molecules and favoring surface reactions. This enhanced surface reactivity may enhance the overall photocatalytic performance of BWO.[85] To summarize, the structure of BWO, comprising its layer morphology, surface defects, crystal facets and band structure collectively affect its photocatalytic capacity. These structural properties define the performance of the material in light uptake, charge separation and redox reactions, thus ultimately impacting its capability as a photocatalyst. Nevertheless, as a photocatalyst, BWO has the same problems: the recombination rate of photo-induced holes and electrons of BWO is still high, the BWO can only adsorb visible light having wavelength shorter than 450 nm because of the band gap restriction.[15,86] Hence, optimization of the aforementioned properties of BWO photocatalyst is the main key to improve its photocatalytic performance.

4.2. Photocatalytic properties of pure and substituted BWO

For some years, bismuth tungstate has been considered as a potential solar energy converter,[87] which can activate the degradation of organic matter[88] through surface redox mechanisms. Despite recent studies, the reaction mechanisms remain complex and poorly understood. In general, several researchers agree that photocatalysis corresponds largely to an oxidation phenomenon governed by the holes (h^+) of the valence band, and likely to be influenced by the presence of certain ions (SO_4^{2-}, HCO^{3-}, NO^{3-}, Na^+, K^+, Ca^{2+}, Mg^{2+}, Cl^-, Cu^{2+}, Fe^{3+}) at variable concentration in aqueous medium.[89] In recent times, $CdWO_4$, $PbWO_4$, $ZnWO_4$, and Ag_2WO_4 have been utilized for photocatalysis because of their favorable electronic band structures that promote chemical reactivity and facilitate the production of free radicals in aqueous suspensions.[90–94] Nevertheless, the practical application of these materials in the visible range is hindered by their high gap energy.

The valence band of Bi_2WO_6 consists of a hybridization of O 2p and Bi 6p orbitals with a minor contribution from Bi 6s orbitals, while the conduction band is primarily composed of 5d tungsten orbitals with a slight contribution from Bi 6p orbitals, as revealed by theoretical studies on its electronic band structure (Fig. 8).[6,95] This results in a widely dispersed valence band that enhances the mobility of photon-excited holes and facilitates oxidation reactions. Bi_2WO_6 has demonstrated great potential in selective organic synthesis and bacterial inactivation in aqueous solutions under visible light, such as benzyl alcohol oxidation to aldehydes and glycerol oxidation to dihydroxyacetone, according to previous.[7,96] Various hierarchical morphologies of Bi_2WO_6 have been synthesized using classical methods, including sol–gel, hydrothermal/solvothermal, combined sol–gel/hydrothermal, and sonochemical methods, producing nanosheets, globules, bowl shapes, peony flowers, microspheres, nanolaminars, hollow structures, microdisks, and multilayer disks.[97–99] These morphologies possess large specific surface areas, facilitating the adsorption of organic molecules and promoting photodegradation. Despite its versatility, Bi_2WO_6 has limitations such as low light absorption capacity, limited response to visible light, and high degree of recombination of charge carriers that hinder its use in

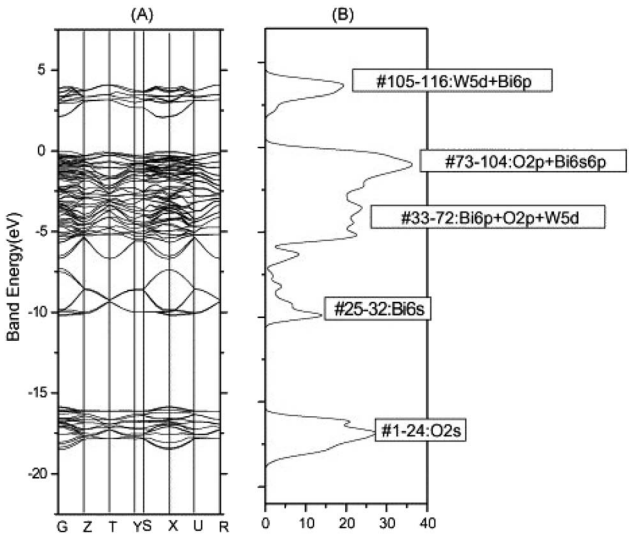

Fig. 8 Bi_2WO_6: (A) band structure, (B) density of states calculated by the DFT method (reproduced from ref. 95 with permission from Elsevier, Copyright 2006).

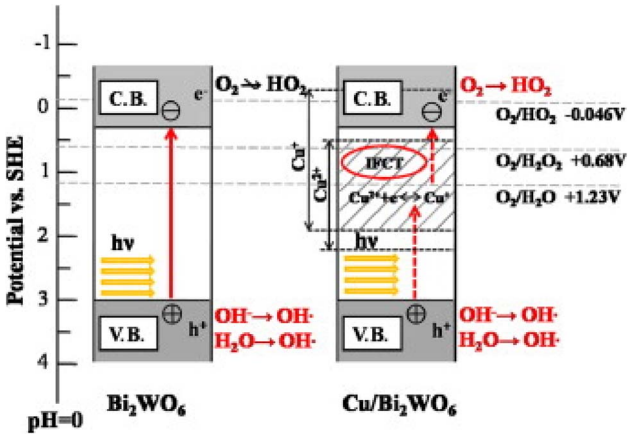

Fig. 9 The photocatalytic mechanism of pure BWO and BWO doped with copper (reproduced from ref. 100 with permission from Elsevier, Copyright 2014).

photocatalysis. Possible modifications to overcome these limitations are discussed below.

The separation of charge carriers could be improved by modifying the surface of Bi_2WO_6 with copper ions (Fig. 9)[100] and by using the synthesis of {0 1 0} reactive facets.[101] This separation of electron–hole pairs, essential for reduction and oxidation reactions, allows the generation of reactive oxygen species. The crystalline facets provide larger surfaces for active sites for photocatalysis.

4.2.1. Metals coupled-Bi_2WO_6. Although doping with noble metals such as silver can prevent recombination of conduction band electrons,[102,103] the Ag–Bi_2WO_6 material exhibits photoactivity even at temperatures between 50–70 °C due to the thermal effects induced by surface plasmon resonance. This suggests that the composite can function as a photocatalyst at higher-than-room temperatures. The combination of the Ag–Bi_2WO_6 composite with mesoporous carbon or graphene has also resulted in excellent radiation adsorption capacity and improved photoactivity.[104,105] In addition, silver nanoparticles are highly effective in scattering and light absorbing properties, and their hybrid effect enhances the spectral range. Moreover, the high conductivity of the carbonaceous structures enables better separation of electron–hole pairs, improving surface reactivities and delaying their recombination. In this context, Chang and his team[106] succeeded in fabricating the Ag–BWO hybrid *via* an electrochemical method. They demonstrated that the contact between BWO, the Ag nanoparticles (NPs) and the substrate helped to effectively separate the photo-excited charges resulting in enhanced photocatalytic activities. In addition, they confirmed that decorated Ag NPs extend the absorption range of UV light to the visible light wavelength region.[106] Recently, a novel Ag-doped BWO/BiOI photocatalyst has been produced using a two-step hydrothermal process. It was observed that the quantity of Ag in BWO/BiOI obviously influenced the photoelectric characteristics and photocatalytic performance.[107] On the other hand, Yang *et al.*[108] attempted to combine Ag with AgCl and BWO to form a ternary system capable of degrading toluene. They demonstrated that the plasmonic effect of silver and high redox performance of the Z-heterojunction significantly enhanced the separation of photo-induced electron/hole pairs and the transfer efficacy.[108] Shen *et al.*[109] have successfully engineered a peony shaped hierarchical 3D Ag/BWO photocatalyst *via* a hydrothermal approach. The possible mechanism discussed in their study suggests that the improved photocatalytic activity derives from the unique morphology of the material, which enables the adsorption of organic substances, and also from the raised Schottky barriers separating the interface of the Ag NPs and BWO, which favor the transfer of photo-induced electrons from BWO to the Ag NPs.[109] The Au–Bi_2WO_6 composite was observed to exhibit photocatalytic activity only when exposed to photons within the 400–800 nm wavelength range, while it remained unresponsive under photon excitation within the 500–800 nm range, despite the existence of surface plasmon resonance of gold nanoparticles in this range. This suggests that there is no direct correlation between the plasmon absorption of gold nanoparticles and the photocatalytic efficiency, as reported by.[110] Furthermore, in another study the excellent photocatalytic activities of Au–BWO composite were attributed to the increased light harvesting efficacy caused by the addition of gold and the high separation of photo-generated electron–hole pairs.[111] Li *et al.*[112] indicated that the surface plasmon resonance effect facilitated photo-generated electron transfer between BWO and Au, leading to accelerated charge transmission and thus inhibiting electron/hole recombination, conferring high photocatalytic properties to the photocatalyst.[112] Similarly, wan *et al.*[113] reported that the inclusion of gold in the BWO@MoS_2 structure allowed the creation of additional charges, which were subsequently passed on to the MoS_2 nano-sheets through S–O conferring high photocatalytic properties to the hybrid. In addition, superior photocatalytic yields have also been ascribed to the effective steering of the charge kinetics implied in this system, notably the HEI (hot electron injection) effect with its extended spectral response range to light for enhanced charge generation.[113] Recently Phuruangrat *et al.*[114] have noted that gold with oxidation degree 3+ was successfully embedded in the BWO lattice, in this investigation they reported that BWO doped with 3% Au has the weakest emission intensity and excellent absorption properties in the UV-visible range with an absorption peak of 437 nm.[114] In another research, Hu *et al.*[115] exploited the optical characteristics of gold to improve the infrared light absorption of BWO. This upgrade was credited to SPR effects and large-scale collection of infrared light using Au nanorods.[115]

4.2.2. Metals ions doped-Bi_2WO_6. Chemical substitution (or doping) influences the arrangement of atoms within the structure, modifies the chemical bonds and thus the band structure of substituted compounds of the type $Bi_{2-x}M_xWO_6$ where M is a trivalent ion (Lu^{3+}). This substitution also plays a role in the crystal growth during synthesis, and can therefore induce various morphological modifications[110] that can be useful for photocatalytic reactions.

The addition of Zr^{4+} metal ions to the Bi_2WO_6 matrix, instead of W^{6+}, can induce an extrinsic oxygen gap by charge compensation, which results in a significant red shift in the band gap

absorption.[116] These oxygen gaps can easily trap excited electrons and prevent charge carrier recombination. Furthermore, these oxygen vacancies can enhance oxygen adsorption on the semiconductor surface, which facilitates the reduction of dioxygen to form superoxide radicals.[117] According to[118] doping with Europium was the primary reason for the high activity of the photocatalyst, rather than changes in band gap absorption properties. Recently, Tahir and his team[119] reported on the *in situ* hydrothermal engineering of a Mn-doped Bi_2WO_6–GO/MoS_2 photocatalyst. They found that the Mn-doped composite had an absorption edge located in the visible zone with a gap energy of 2.2 eV. Additionally, the Mn-doped BMG displayed an even larger light absorption region in the entire visible domain when compared to the virgin ternary sample. In the same year, Su *et al.*[120] succeeded in making Ni^{2+}/Bi_2WO_6 with a flower shape. The characterization findings showed that Ni^{2+} was able to penetrate into Bi_2WO_6 and partly supplant Bi^{3+}. Furthermore, the improvement of photocatalytic properties is attributed to the creation of defects and the reduction of the gap in the Ni^{2+}–Bi_2WO_6. Photocatalytic findings revealed that the highest photocatalytic breakdown rate of RhB, up to 93%, was attained when using 0.25% Ni^{2+}–Bi_2WO_6. In another similar work by ref. 121, have shown that Bi^{5+} doping allows to narrow the bandgap of Bi_2WO_6 nano-flowers, and enhances the absorption capability of Bi_2WO_6 nano-flowers in the visible-light rang significantly. A Bi_2WO_6 doped Bi–I photo-catalyst was successfully produced through a solvothermal process. The superior photoactivity of the I-doped Bi_2WO_6 photocatalyst was mainly attributed to two factors: the introduction of impurity levels by the I dopant, which enhanced visible light absorption, and the efficient migration and separation of charge carriers. Additionally, the surface plasmon resonance (SPR) effect of the Bi metal also contributed significantly to the improvement in photocatalytic activity, as reported by ref. 121.

A comparative study was carried out by Zhu *et al.*[122] in which they compared the photocatalytic performances of Bi_2WO_6 doped with various metals ions such as (Cu^{2+}, Zn^{2+}, Mg^{2+} and Fe^{3+}). They have found that Bi_2WO_6 doped with metal ions greatly enhances the photodecomposition of ciprofloxacin (CIP) and norfloxacin (NOR) antibiotics, this improvement was explained by the increase of the specific surface area after doping and the reduction of the gap energies (novel impurity levels entered between the CB and the VB of Bi_2WO_6). Furthermore, they found that Mg^{2+} doped as an electron reservoir allowed the Mg/Bi_2WO_6 composite to have the highest degradation rate of 99.11% for CIP and 89.44% for NOR. On the other hand, iron doping displayed a plasmonic resonance effect and consequently a strong absorption of visible light was noted.[122] In a related study, Lovisa *et al.*,[123] reported the manufacture of zinc-doped Bi_2WO_6. In this study they demonstrated that increasing the Zn^{2+} concentration promoted the inhibition of photocatalytic characteristics through the occurrence of oxygen vacancies that functioned as a charge recombination center. On the other hand, the photoluminescence was further enhanced by the Zn^{2+} doping, moreover the color adjustment was favored according to the increase in zinc content noticing the transition from: yellow to orange to green. Bera and his co-authors,[124] proved that *in situ* doping of the Bi_2WO_6 microstructure with a metal (Fe, Zn, Mo) has improved the absorption and charge transfer efficacy. It was revealed that Mo doping displayed the strongest photocurrent density, which was 57 fold better compared to that of naked Bi_2WO_6. In addition, the smaller ionization potential for Mo–Bi_2WO_6 indicated an enhancement in electron mobility and charge separation. On the other hand, Koteski *et al.*[125] have exploited density functional theory to investigate substitutional doped $Bi_2W_{1-x}M_xO_6$ with (M = Mo, Fe, Cr, Zn; $x = 0.125, 0.50, 0.25$). They found that for all transition metal dopants examined, the optical characteristics in the visible spectrum were superior to those of non-doped Bi_2WO_6 (Fig. 10a). This improvement was explained by the localized defective states in the bandgap upon insertion of Fe, Mo and Cr which leads to the narrowing of the bandgap. In addition, as shown in Fig. 10b Zinc doping exhibited more enhanced optical properties compared to other dopants as it eased the narrowing of the band gap through inducing a shift of the states close to the peak of the valence band to higher energies. In another study a series of Cu^{2+}/Ni^{2+} doped Bi_2WO_6 was manufactured with success *via* a simple solvothermal procedure and it displayed the highest photocatalytic ability with low charge transfer resistance and considerable photocurrent.[126] Zhong *et al.*[127] demonstrated that after the insertion of copper into the Bi_2WO_6 structure the absorption edge was dramatically enhanced and moved to the red in the visible zone, which was ascribed to the charge transfer between the Cu species and the host matrix. Moreover, the inclusion of copper ions in the BWO structure has introduced some new energy levels of the copper ions within the band gap of BWO, leading to a diminished band gap. In a related study, iron doping exhibited a lower emission intensity in comparison to the non-doped Bi_2WO_6, which confirmed that the iron effectively suppressed the charge recombination. Additionally, Fe-BWO gave a greater photocurrent response and a reduced charge transfer resistance. It was observed that the increase in iron concentration led to an increase in PL intensity, this was accounted for by the fact that the surplus oxygen vacancies might function as hole–electron recombination centers[128] Arif *et al.*[129] indicated that titanium (Ti) doping has a significant impact on the band structure and electron dynamics, and also was able to insert redox couples (Ti^{3+}/Ti^{4+}), leading to a meaningful increase in reactive oxygen entities during the photocatalytic process, in addition to the Ti doping may also produce crystal defects in the crystal lattice of BWO, leading to highly improved visible-light driven photocatalytic activity. Optical results showed that Ti doping exhibited an apparent blue shifting (about 18 nm), which might be attributed to the substitution of Bi^{3+} by the Ti^{3+} cation and the nano-scale (NS) effect, in addition to which a weaker PL emission intensity was found for the Ti-doped Bi_2WO_6 pointing to a low rate of recombination of the photo-induced hole–electron pairs. In addition, the presence of Ti cations upon the surface of BWO might function as an oxygen scavenging site, thus benefiting redox pair generation and the interfacial charge transfer, thereby resulting in improved photocatalytic efficiency.[129] In order to achieve improved photocatalytic properties of Bi_2WO_6, the same team controlled the Ti

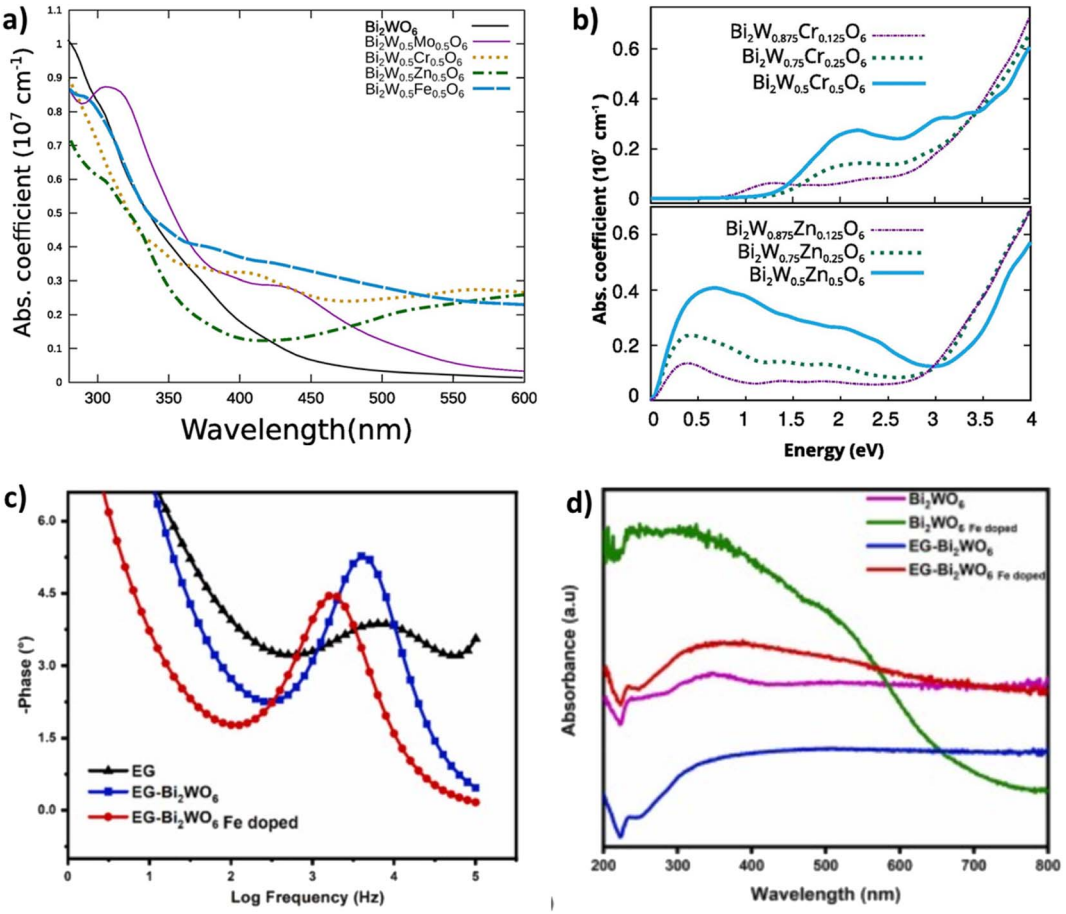

Fig. 10 (a and b) DRS analysis and absorbance coefficients of doped and non-doped BWO (reproduced from ref. 125 with permission from Elsevier, copyright 2020). (c) EIS experiments of EG, EG-BWO and EG-Fe doped BWO electrodes. (d) DRS spectra of doped and doped BWO (reproduced from ref. 131 with permission from Elsevier, Copyright 2022).

dopant level to alter the crystal defects and oxygen vacancies in the Bi_2WO_6 crystal lattice. It was shown that the crystal defects mediated *via* Ti doping and generated oxygen vacancies were critically significant for controlling the photocatalytic behavior of Bi_2WO_6. Remarkably, the Ti–Bi_2WO_6 hybrid displays deeply enhanced photocatalytic activity for the decomposition of ceftriaxone sodium and an especially enhanced photocatalytic H_2 yield, with a 5.8 times higher rate than Bi_2WO_6.[130] Mahhumane and co-authors,[131] documented that iron doping gave superhydrophilicity to Bi_2WO_6 and resulted in better charge separation. As shown in Fig. 10c, electrochemical impedance spectroscopy experiments showed that switching the EG-Fe-doped BWO electrode to a slower frequency confirms a more rapid electron transport process. Furthermore, the influence of Fe-doping was visible through the increased absorbance in comparison to the electrode not doped by Fe (Fig. 10d). This indicated that Fe doping enhances the photoresponse of BWO. It was noted that the gap energy of Bi_2WO_6 and iron doped Bi_2WO_6 was 2.7 eV and 1.6 eV respectively, this reduction was due to the creation of an iron doping level in the band gap of BWO, which helped to separate holes and electrons.[131] New Co-doped Bi_2WO_6 nano-sheets onto the surfaces of a Fe_3O_4 composite material were successfully produced using a facile hydrothermal approach, it was suggested that the enhancement of photocatalytic properties was attributed to the effect of Co^{2+} doping as well as the synergistic action between the heterojunction interface, which gave rise to high visible light uptake with a great charge separation efficacy. The PL results indicated that the fabricated composite showed noticeably low emission intensity, suggesting a weaker recombination rate of photo-induced electrons/holes. Furthermore, gap energy calculations indicated that the doped Bi_2WO_6 exhibited a gap energy of 2.75 eV which was 0.06 eV shorter compared to that of pristine Bi_2WO_6.[132]

4.2.3. Doping with RE elements. According to research by ref. 133, rare earth ions including Ce^{3+}, Nd^{3+} are effective dopants for promoting photocatalytic activity, while Pr ions show poor efficiency. Rare earth-modified Bi_2WO_6 composites (RE/Bi_2WO_6) also show great potential as Bi_2WO_6 dopants. The rare earth series, consisting of 17 rare earth elements including Sc, Y, and lanthanides (La to Lu), are known for their unique electronic and optical properties and have been extensively studied for their photocatalytic performance due to their rich energy level structures and strong multi-band emission.[134,135] They can be incorporated into the Bi_2WO_6 crystal lattice by replacing Bi^{3+} ions, leading to the formation of RE-Bi_2WO_6 solid

solutions. This incorporation of RE^{3+} ions can act as electron traps, which can extend the lifetime of photogenerated charge carriers (electrons and holes) and improve their separation efficiency. In addition, RE^{3+} ions can also change the band structure of the material, leading to a shift in band gap energy and an increase in visible light absorption.[136] This in turn can lead to an improvement in the overall photocatalytic performance of the material. Furthermore, as each rare earth element has its own electronic structure and properties, the specific properties of the modified Bi_2WO_6 will depend on the type of RE^{3+} ion used; this renewed interest in rare earth has led to many research efforts dedicated to the preparation of new types of Bi_2WO_6 nanomaterials for photocatalytic applications.[137] In particular, different modification strategies have been successfully used to improve the photocatalytic properties of Bi_2WO_6 nanomaterials.

4.2.3.1 Single rare-earth doping. Different Bi_2WO_6 composite photocatalysts have been doped with a single rare earth that has shown great promise in enhancing the photocatalytic activity and other properties of Bi_2WO_6, making it an attractive option for researchers studying photocatalytic reactions. For instance, Tian *et al.*[138] used a hydrothermal process to validate that Gd/Bi_2WO_6 has higher potential applications in various fields such as photocatalysis, optoelectronics, and energy storage. However, further research is needed to fully understand its properties and optimize its performance for specific applications. Ahsaine *et al.*,[139] Successfully fabricated a composite by a co-precipitation method that showed enhanced photocatalytic activity under UV light irradiation, as the lutetium dopant can reduce the band gap of Bi_2WO_6, which facilitates the absorption of UV light and can increase the number of electron–hole pairs generated in the material. Indeed, the lutetium dopant can improve the charge separation and stability to reduce the electron–hole recombination rate and enhance the overall photocatalytic efficiency of the material. Similarly, the related research of doped tungstate matrix rare earth is numerous such as Guo and Ren[140] elaborated the photocatalyst Tb^{3+} doped Bi_2WO_6 by a co-precipitation method and studied their luminescence properties. Gu *et al.*[141] synthesized Eu/Bi_2WO_6 by a hydrothermal process, which can effectively improve the photostability of Bi_2WO_6 nanoparticles making them suitable for use in long-term applications.[142] prepared 3D hierarchical flower-shaped microspheres of Sm^{3+}-doped Bi_2WO_6 and found that the 0.5% Sm-BWO sample exhibited the best adsorption capacity among the materials studied due to the synergistic effect of a suitable band gap and high specific surface area. Since Bi_2WO_6 is considered relatively safe and non-toxic, this makes it, along with Sm^{3+}, a potentially attractive material for biomedical applications and could also lead to promising candidates for a wide range of applications, especially in photocatalysis and optoelectronics.[133] synthesized and compared the photocatalytic activity of doped Bi_2WO_6 (Ce^{3+}, Nd^{3+}, Pr^{3+} or Sm^{3+}) *via* a facile hydrothermal process. The result of all these samples is that Nd^{3+} in Bi_2WO_6 enhanced the photocatalytic activity with 99.8% degradation of RhB dye after 20 minutes of irradiation. In this context[143] doped La, Ce, Gd, and Yb *via* simple hydrothermal method into the catalyst; the results showed that Gd and Yb are the best for improving their catalytic ability. The more 4f electrons in Gd and Yb cause a stronger distortion of the crystal lattice, which affects the position of the valence band maximum and conduction band minimum. This leads to a larger bandgap and a red shift of the absorption edge to the visible light region. In contrast, La/Bi_2WO_6 and Ce/Bi_2WO_6 do not have as many 4f electrons, and therefore, their crystal lattice distortion is not as strong, resulting in a smaller bandgap and a weaker red shift to the visible light region (Fig. 11a and b). Compared to the doping amount of 2% Yb/Bi_2WO_6 presented by ref. 144 shows that 2% Yb significantly enhances the visible light absorption properties of the material and can act as an electron acceptor that facilitates the electron transfer from the conduction band of Bi_2WO_6 to the Yb ions, leading to better improvements in photocatalytic performance. Photoluminescence analysis (Fig. 11c) showed that the emission capacity of the Yb–BWO hybrid catalysts was considerably decreased relative to that of the original BWO, and the intensity of 2.0%Yb–BWO was the lowest. In addition, compared to BWO, the Yb–BWO compound exhibits a greater photocurrent response (Fig. 11d), which is coherent with lower fluorescence and greater photo-activity. Recently,[145] showed that the 1% flower-shaped Pr–Bi_2WO_6 microspheres prepared by one-step hydrothermal method exhibited the best photocatalytic performance to degrade RhB based on radical scavenging experiments. Besides to Pr,[146] employed 16% Er^{3+}–Bi_2WO_6 heterostructure photocatalysts to break down tetracycline which can be used for longer periods without losing its effectiveness.

4.2.3.2 Co-doping with rare-earths. While doping Bi_2WO_6 with other elements is not a novel idea, there are few studies on rare earth co-doping with Bi_2WO_6. In a study by ref. 147, Yb^{3+}/Ho^{3+}-Bi_2WO_6 was synthesized using a hydrothermal method and a heat treatment process, which demonstrated good upconversion luminescence, exceptional photocatalytic activity, and stability in degrading RhB solution under visible light exposure. Similarly,[148] found that Yb^{3+}/Nd^{3+}-Bi_2WO_6 prepared through the hydrothermal approach offered several benefits over single doping. The Yb^{3+}/Nd^{3+} addition acted as electron traps, facilitating charge transfer and reducing recombination of photoinduced electron–hole pairs. Moreover, the addition of 1.5% Yb^{3+} and 0.5% Nd^{3+} in the Bi_2WO_6 crystal lattice generated more oxygen vacancies, thereby increasing the yield of O_2^- and restraining electron–hole pair recombination, ultimately enhancing the photocatalytic performance.[149] created Bi_2WO_6: Er, Yb nanofibers through the solvothermal-electrospinning approach, which displayed great compatibility between crystal and nanofiber. The Yb^{3+} ions served as sensitizers to absorb photons and transfer energy to Er^{3+} ions, absorb near-infrared light and transfer energy to Bi_2WO_6, thus increasing the number of electron–hole pairs and improving photocatalytic activity. Recently,[150] produced and employed Bi_2WO_6 through a hydrothermal process. The literature suggests that co-doping Nd and Pr in Bi_2WO_6 can enhance photocatalytic activity under visible light irradiation by improving its light responsiveness, enlarging the specific surface area of the photocatalyst, and

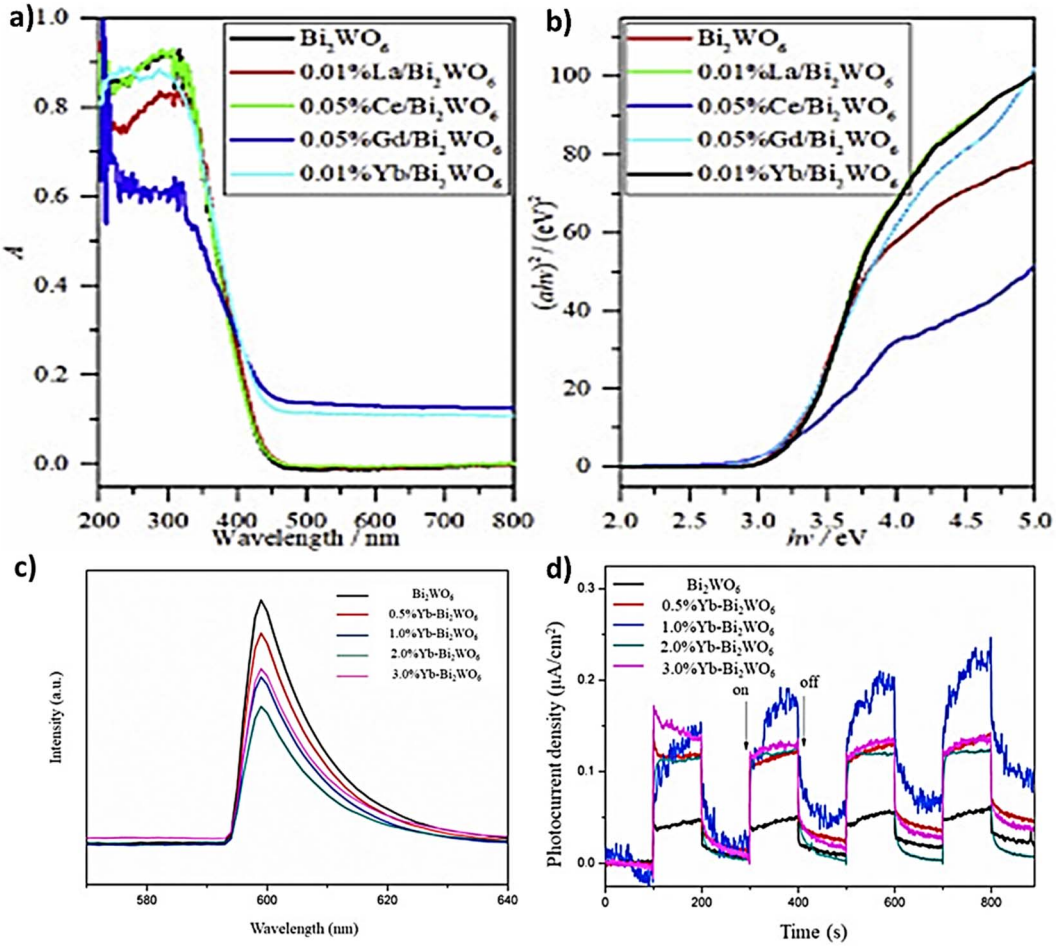

Fig. 11 (a and b) DRS and Tauc's spectra of doped and non-doped BWO (reproduced from ref. 143 with permission from Elsevier, copyright 2021). (c) PL spectra of BWO doped by different Yb concentration. (d) Photocurrent responses of pristine and doped BWO (reproduced from ref. 144 with permission from Elsevier, copyright 2021).

decreasing the recombination rate of electrons and photogenerated holes, making it useful for degrading contaminants.

4.2.3.3 Triple-doping with rare-earths. Besides, co-doping RE, many research efforts have been devoted to the preparation of a new photocatalysis strategy. Recently, a publication by ref. 151 produced a new Bi_2WO_6 with triple doping of Yb, Er and Pr *via* a hydrothermal process, which exhibits superior performance in photocatalytic activity compared to Bi_2WO_6 doped with a single and co-dopant. The collaborative effect between the three rare earth dopants can act as an electron-trapping center to produce more O^{2-} radicals and promote electron–hole pair separation. In addition, the material exhibits good stability and durability, as well as a wide band gap, making it an attractive option for researchers investigating photocatalytic materials as new candidates for a range of advanced technological applications.

4.2.4. Doping with other elements. In this section, the research data also shows the practical use of other doped elements to achieve their goal. They have successfully used different modification strategies to improve the photocatalytic efficiency of these elements in various applications. The following are some of the commonly used dopants for Bi_2WO_6. Incorporating nitrogen, boron, and iodine as dopants has been shown to enhance the photocatalytic activity of Bi_2WO_6. Although boron can improve the catalyst's acidity, it has a limited response to visible light Bi_2WO_6, as noted by ref. 152 and 153. However, due to its electron-deficient nature, boron can capture electrons to eliminate recombination channels and act as an electron scavenger, promoting the separation of photogenerated electron–hole pairs and thus improving photocatalytic efficiency. Iodine was used as an insertion dopant because of the presence of multivalent species (I_0 and I^-) in the host matrix. During photocatalysis, I_0 acts as an electron acceptor and becomes I^-, while hole trapping leads to simultaneous re-oxidation. Additionally, the high concentration of oxygen vacancies and reduction of tungsten from the 6+ to 4+ state can reconfigure the internal local electric field, which promotes charge carrier separation.

Recently, self-doping with bismuth ions (Bi^{4+} or Bi^{5+}) and with cerium–fluorine elements (Ce–F) have been reported in the literature in order to obtain better photoactivity.[154,155] The introduction of self-dopants such as Bi^{3+} or Bi^{5+} promoted the

generation of superoxide radicals and boosted the density of charge carriers. Meanwhile, doping with cerium caused a blue-shift in the absorption spectrum of the synthesized material, while the incorporation of fluorine expanded the spectral response. When multiple species were modified simultaneously, synergistic effects emerged that facilitated the separation of charge carriers and accelerated the degradation of pollutants.

Boron, being a metalloid with properties of both metals and nonmetals, has been successfully doped into Bi_2WO_6 using a hydrothermal method, as reported in ref. 156. The addition of 0.5% B/Bi_2WO_6 has shown an increase in mesopores and pore volume, leading to stronger catalytic activity under simulated solar light for degradation. Other studies, such as,[152,157] have used a hydrothermal process and a two-step and microwave-assisted hydrothermal method, respectively, to achieve N-doping of Bi_2WO_6. However, it has been observed that increasing the dopant concentration leads to an increase in the recombination rate, resulting in decreased efficiency. On the other hand,[158] found that I-doping into Bi_2WO_6 nanosheets is effective in the photocatalytic removal of Hg^0, as it enhances visible light absorption, generates higher electron–hole pairs, and improves the selectivity of Bi_2WO_6 for Hg_0 removal, making it a promising product for environmental remediation applications. Recently,[159] synthesized P-doped and S-doped Bi_2WO_6 by hydrothermal treatment of Bi_2WO_6 nanosheets. S-doped Bi_2WO_6 was found to have a higher ability to adsorb CO_2 than P-doped Bi_2WO_6, as it increases the surface area and the number of active sites available for CO_2 adsorption. The presence of S in Bi_2WO_6 also leads to the formation of oxygen vacancies and stronger chemical bonds between Bi_2WO_6 and CO_2, providing a useful strategy to further optimize the photocatalytic performance of Bi_2WO_6 for future applications.

5. Conclusion, challenges and perspectives

In conclusion, in this review we have provided a detailed structural study of the Bi_2WO_6 and its isotypic materials. This material has a promising electrical, and photoluminescent properties which explains its wide use a range of purposes including capacitors, humidity detectors, optical sensors, and thermistors. Bismuth tungstate has shown promising photocatalytic activity for water treatment and dye photocatalysis applications both in its bare and doped configurations. Doping with noble metals such as silver or rare earth elements such as Yb^{3+}, Ho^{3+}, Nd^{3+}, and Pr^{3+} can further enhance the photocatalytic performance of Bi_2WO_6 by facilitating charge transfer and reducing the recombination of photoinduced electron–hole pairs. However, the practical application of Bi_2WO_6 as a photocatalyst for water treatment is still limited by several challenges as follows:

(a) High recombination rates: the recombination rate of photoinduced electron–hole pairs is high, which reduces the efficiency of photocatalytic degradation.

(b) Narrow light absorption range: bismuth tungstates have limited light absorption in the visible region, which limits their use in practical applications.

(c) Low quantum efficiency: bismuth tungstates have a low quantum efficiency, meaning that only a small fraction of the absorbed photons is converted into electron–hole pairs, resulting in low photocatalytic efficiency.

(d) Difficulty in synthesis: the synthesis of bismuth tungstates can be challenging and time-consuming, limiting their large-scale production.

Some of the potential solutions and strategies to overcome these drawbacks are as follow:

Doping bismuth tungstates with metals or non-metals can improve their photocatalytic properties, such as enhancing their visible light absorption and reducing recombination rates.

Introduction of co-catalysts to further improve the photocatalytic activity of bismuth tungstate. Noble metals (such as Pt, Au) or co-catalysts such as cocooning agents, metal oxide nanoparticles, and carbon-based materials have been employed to promote charge transfer and increase the effectiveness of particular reactions.

Engineering of nanostructures by increasing surface area to improve light harvesting efficiency was also reported.

Facets engineering to obtain highly photoactive facets for photoconversion applications.

New experimental and computational methodologies have improved our comprehension of the photocatalytic processes of bismuth tungstate. To maximize the effectiveness and performance of bismuth's photocatalytic properties, scientists are examining the particular functions of defect engineering, surface states, and band locations.

Optimization of synthesis conditions such as temperature, time, and reactant concentration can improve the photocatalytic performance of bismuth tungstates.

However, there is a need for further studies on the underlying mechanisms of photocatalytic activity using operando investigation, the development of more efficient and stable bismuth tungstate-based photocatalysts, and the exploration of new applications in fields such as water treatment and energy conversion.

Conflicts of interest

The authors declare that they have no competing interests.

References

1 G. Zhao, S. Hao, Y. Xing, Y. Wang, Y. Wang, K. Xu and X. Xu, *Phys. Status Solidi A*, 2019, **216**, 1900035.
2 K. Zhang, J. Wang, W. Jiang, W. Yao, H. Yang and Y. Zhu, *Appl. Catal., B*, 2018, **232**, 175–181.
3 H. Ait Ahsaine, A. BaQais, M. Arab, B. Bakiz and A. Benlhachemi, *Catalysts*, 2022, **12**, 1335.
4 Y. Li, J. Liu and X. Huang, *Nanoscale Res. Lett.*, 2008, **3**, 365–371.
5 A. Kudo and S. Hijii, *Chem. Lett.*, 1999, **28**, 1103–1104.
6 J. Tang, Z. Zou and J. Ye, *Catal. Lett.*, 2004, **92**, 53–56.

7 J. Ren, W. Wang, L. Zhang, J. Chang and S. Hu, *Catal. Commun.*, 2009, **10**, 1940–1943.
8 H. Fu, C. Pan, W. Yao and Y. Zhu, *J. Phys. Chem. B*, 2005, **109**, 22432–22439.
9 Z. Liu, B. Wu, J. Niu, X. Huang and Y. Zhu, *Appl. Surf. Sci.*, 2014, **288**, 369–372.
10 H. Ait Ahsaine, M. Ezahri, A. Benlhachemi, B. Bakiz, S. Villain, F. Guinneton and J.-R. Gavarri, *Ceram. Int.*, 2016, **42**, 8552–8558.
11 S. O. Alfaro and A. Martínez-de la Cruz, *Appl. Catal., A*, 2010, **383**, 128–133.
12 Z. He, C. Sun, S. Yang, Y. Ding, H. He and Z. Wang, *J. Hazard. Mater.*, 2009, **162**, 1477–1486.
13 K. Tekintas, Ö. Kesmez, O. Bekircan and E. T. Saka, *J. Mol. Struct.*, 2022, **1248**, 131405.
14 W. Nachit, H. Ait Ahsaine, Z. Ramzi, S. Touhtouh, I. Goncharova and K. Benkhouja, *Opt. Mater.*, 2022, **129**, 112256.
15 L. Zhang and Y. Zhu, *Catal. Sci. Technol.*, 2012, **2**, 694–706.
16 F. Amano, K. Nogami and B. Ohtani, *Catal. Commun.*, 2012, **20**, 12–16.
17 K. S. Knight, *Mineral. Mag.*, 1992, **56**, 399–409.
18 T. Zeng, H. Yan, H. Ning, J. Zeng and M. J. Reece, *J. Am. Ceram. Soc.*, 2009, **92**, 3108–3110.
19 H. Yi, L. Qin, D. Huang, G. Zeng, C. Lai, X. Liu, B. Li, H. Wang, C. Zhou, F. Huang, S. Liu and X. Guo, *Chem. Eng. J.*, 2019, **358**, 480–496.
20 X. Liu, S. Gu, Y. Zhao, G. Zhou and W. Li, *J. Mater. Sci. Technol.*, 2020, **56**, 45–68.
21 T. Chen, L. Liu, C. Hu and H. Huang, *Chin. J. Catal.*, 2021, **42**, 1413–1438.
22 L. Zhang, W. Wang, L. Zhou and H. Xu, *Small*, 2007, **3**, 1618–1625.
23 M. Shang, W. Wang, L. Zhang, S. Sun, L. Wang and L. Zhou, *J. Phys. Chem. C*, 2009, **113**, 14727–14731.
24 C. Wu, J. Zhong, J. Xie, D. Wang, Y. Shi, Q. Chen, H. Yan and J. Zhu, *Appl. Surf. Sci.*, 2019, **484**, 112–123.
25 A. J. J. Amalraj and S.-F. Wang, *Colloids Surf., A*, 2022, **648**, 129183.
26 W. Guo, L. Jian, X. Wang and W. Zeng, *Sens. Actuators, B*, 2022, **357**, 131396.
27 Y.-Q. Wang, C. Yang and L.-H. Gan, *Int. J. Hydrog. Energy.*, 2023, **48**, 19372–19384.
28 Z. Lin, Z. Yang and J. Huang, *Beilstein J. Nanotechnol.*, 2022, **13**, 745–762.
29 T. Liu, F. Xue, B. Wang, R. Wang, W. Cao, X. Zhao, Y. Xia, W. Jin, Y. Zhang and H. Lin, *J. Catal.*, 2023, **417**, 41–51.
30 Y. Hu, J. Fan, C. Pu, H. Li, E. Liu and X. Hu, *J. Photochem. Photobiol., A*, 2017, **337**, 172–183.
31 D. Lv, D. Zhang, X. Pu, D. Kong, Z. Lu, X. Shao, H. Ma and J. Dou, *Sep. Purif. Technol.*, 2017, **174**, 97–103.
32 T. Ji, E. Ha, M. Wu, X. Hu, J. Wang, Y. Sun, S. Li and J. Hu, *Catalysts*, 2020, **10**, 1161.
33 T. Cadenbach, M. J. Benitez, A. L. Morales, C. C. Vera, L. Lascano, F. Quiroz, A. Debut and K. Vizuete, *Beilstein J. Nanotechnol.*, 2020, **11**, 1822–1833.
34 Y. Hao, Z. Tian, C. Liu and C. Xiao, *Front. Chem.*, 2023, **11**, 19.
35 N. A. McDowell, K. S. Knight and P. Lightfoot, *Chem.–Eur. J.*, 2006, **12**, 1493–1499.
36 H. Kodama and A. Watanabe, *J. Solid State Chem.*, 1985, **56**, 225–229.
37 G. Sankar, M. A. Roberts, J. M. Thomas, G. U. Kulkarni, N. Rangavittal and C. N. R. Rao, *J. Solid State Chem.*, 1995, **119**, 210–215.
38 D. J. Buttrey, T. Vogt, U. Wildgruber and W. R. Robinson, *J. Solid State Chem.*, 1994, **111**, 118–127.
39 P. Bégué, R. Enjalbert, J. Galy and A. Castro, *Solid State Sci.*, 2000, **2**, 637–653.
40 V. I. Voronkova, E. P. Kharitonova and O. G. Rudnitskaya, *J. Alloys Compd.*, 2009, **487**, 274–279.
41 M. Maczka, L. Macalik, K. Hermanowicz, L. Kępiński and P. Tomaszewski, *J. Raman Spectrosc.*, 2010, **41**, 1059–1066.
42 J. S. Xue, M. R. Antonio and L. Soderholm, *Chem. Mater.*, 1995, **7**, 333–340.
43 O. Beaury, M. Faucher and G. Teste de Sagey, *Acta Crystallogr., Sect. B: Struct. Crystallogr. Cryst. Chem.*, 1981, **37**, 1166–1170.
44 J. A. Alonso, F. Rivillas, M. J. Martınez-Lope and V. Pomjakushin, *J. Solid State Chem.*, 2004, **177**, 2470–2476.
45 A. V Tyulin and V. A. Efremov, *Kristallografiya*, 1987, **32**, 363–370.
46 A. Watanabe, *Mater. Res. Bull.*, 1980, **15**, 1473–1477.
47 P. S. Berdonosov, D. O. Charkin, K. S. Knight, K. E. Johnston, R. J. Goff, V. A. Dolgikh and P. Lightfoot, *J. Solid State Chem.*, 2006, **179**, 3437–3444.
48 H. A. Ahsaine, 2016.
49 A. Taoufyq, H. Ait Ahsaine, L. Patout, A. Benlhachemi, M. Ezahri, F. Guinneton, A. Lyoussi, G. Nolibe and J.-R. Gavarri, *J. Solid State Chem.*, 2013, **203**, 8–18.
50 Z. Zhang, W. Wang, L. Wang and S. Sun, *ACS Appl. Mater. Interfaces*, 2012, **4**, 593–597.
51 H. Takeda, J. S. Han, M. Nishida, T. Shiosaki, T. Hoshina and T. Tsurumi, *Solid State Commun.*, 2010, **150**, 836–839.
52 D. O. Charkin, D. N. Lebedev, S. Y. Stefanovich and S. M. Kazakov, *Solid State Sci.*, 2010, **12**, 2079–2085.
53 M. Mączka, A. F. Fuentes, L. Kępiński, M. R. Diaz-Guillen and J. Hanuza, *Mater. Chem. Phys.*, 2010, **120**, 289–295.
54 T. Šalkus, L. Šatas, A. Kežionis, M. Kodols, J. Grabis, V. Vikhrenko, V. Gunes and M. Barré, *Solid State Ionics*, 2015, **271**, 73–78.
55 S. M. Sze and K. K. Ng, *Physics of semiconductor devices*, John Wiley, NY, 1981, pp. 122–129.
56 V. Nagirnyi, E. Feldbach, L. Jönsson, M. Kirm, A. Lushchik, Ch. Lushchik, L. L. Nagornaya, V. D. Ryzhikov, F. Savikhin, G. Svensson and I. A. Tupitsina, *Radiat. Meas.*, 1998, **29**, 247–250.
57 A. B. van Oosterhout, *J. Chem. Phys.*, 2008, **67**, 2412–2418.
58 V. B. Mikhailik, H. Kraus, G. Miller, M. S. Mykhaylyk and D. Wahl, *J. Appl. Phys.*, 2005, **97**, 083523.
59 V. Nagirnyi, E. Feldbach, L. Jönsson, M. Kirm, A. Kotlov, A. Lushchik, V. A. Nefedov and B. I. Zadneprovski, *Nucl. Instrum. Methods Phys. Res., Sect. A*, 2002, **486**, 395–398.

60 A. E. Ovechkin, V. D. Ryzhikov, G. Tamulaitis and A. Žukauskas, *Phys. Status Solidi A*, 1987, **103**, 285–290.
61 R. Grasser, E. Pitt, A. Scharmann and G. Zimmerer, *Phys. Status Solidi B*, 1975, **69**, 359–368.
62 V. O. Sokolov, V. G. Plotnichenko and E. M. Dianov, *Opt. Lett.*, 2008, **33**, 1488–1490.
63 R. Cao, M. Peng and J. Qiu, *Opt. Express*, 2012, **20**, A977–A983.
64 M. Mączka, A. F. Fuentes, K. Hermanowicz, L. Macalik, P. E. Tomaszewski, L. Kępínski and R. Lisiecki, *J. Nanosci. Nanotechnol.*, 2010, **10**, 5746–5754.
65 Z. J. Zhang and X. Y. Chen, *Mater. Sci. Eng., B*, 2016, **209**, 10–16.
66 O. M. Bordun, *J. Appl. Spectrosc.*, 1998, **65**, 149–151.
67 G. Blasse and G. J. Dirksen, *Chem. Phys. Lett.*, 1982, **85**, 150–152.
68 O. M. Bordun, A. T. Stetskiv and T. M. Yaremchuk, *Ukrainian J. Phys.*, 2004, **49**, 991–995.
69 V. Nagirny, E. Feldbach, L. Jonsson, M. Kirm and A. Kotlov, *Radiat. Meas.*, 1998, **29**, 247–250.
70 G. Blasse, *Luminescence and energy transfer*, Springer, 2005, pp. 1–41.
71 R. Grasser, A. Scharmann and K.-R. Strack, *J. Lumin.*, 1982, **27**, 263–272.
72 V. B. Mikhailik, H. Kraus, G. Miller, M. S. Mykhaylyk and D. Wahl, *J. Appl. Phys.*, 2005, **97**, 83523.
73 H. A. Ahsaine, M. Ezahri, A. Benlhachemi, B. Bakiz, S. Villain, J.-C. Valmalette, F. Guinneton, M. Arab and J.-R. Gavarri, *RSC Adv.*, 2015, **5**, 96242–96252.
74 J.-M. Herrmann, *Catal. Today*, 1999, **53**, 115–129.
75 A. Elaouni, M. E. Ouardi, M. Zbair, A. BaQais, M. Saadi and H. A. Ahsaine, *RSC Adv.*, 2022, **12**, 31801–31817.
76 S. Lotfi, M. E. Ouardi, H. A. Ahsaine and A. Assani, *Catal. Rev.*, 2022, 1–45.
77 M. El Ouardi, A. El aouni, H. A. Ahsaine, M. Zbair, A. BaQais and M. Saadi, *Chemosphere*, 2022, 136483.
78 D. Dvoranová, V. Brezova, M. Mazúr and M. A. Malati, *Appl. Catal., B*, 2002, **37**, 91–105.
79 L. Zhang, H. Wang, Z. Chen, P. K. Wong and J. Liu, *Appl. Catal., B*, 2011, **106**, 1–13.
80 G. Zhang, Z. Hu, M. Sun, Y. Liu, L. Liu, H. Liu, C.-P. Huang, J. Qu and J. Li, *Adv. Funct. Mater.*, 2015, **25**, 3726–3734.
81 Y. Zhou, Y. Zhang, M. Lin, J. Long, Z. Zhang, H. Lin, J. C.-S. Wu and X. Wang, *Nat. Commun.*, 2015, **6**, 8340.
82 R. Liu, Y. Shi, L. Lin, Z. Wang, C. Liu, J. Bi, Y. Hou, S. Lin and L. Wu, *Appl. Surf. Sci.*, 2022, **605**, 154822.
83 Y. Liu, B. Wei, L. Xu, H. Gao and M. Zhang, *ChemCatChem*, 2015, **7**, 4076–4084.
84 L. Wang, C. Guo, F. Chen, J. Ning, Y. Zhong and Y. Hu, *J. Colloid Interface Sci.*, 2021, **602**, 868–879.
85 H. Sun, Z. Tian, G. Zhou, J. Zhang and P. Li, *Appl. Surf. Sci.*, 2019, **469**, 125–134.
86 E. Gao, W. Wang, M. Shang and J. Xu, *Phys. Chem. Chem. Phys.*, 2011, **13**, 2887–2893.
87 B. Y. Alfaifi, A. A. Tahir and K. G. U. Wijayantha, *Sol. Energy Mater. Sol. Cells*, 2019, **195**, 134–141.
88 M. B. Tahir, T. Nawaz, G. Nabi, M. Sagir, M. Rafique, A. Ahmed and S. Muhammad, *Int. J. Hydrogen Energy*, 2020, **45**, 22833–22847.
89 C. Wang, L. Zhu, M. Wei, P. Chen and G. Shan, *Water Res.*, 2012, **46**, 845–853.
90 B. Fatima, S. I. Siddiqui, R. Ahmed and S. A. Chaudhry, *Water Resour. Ind.*, 2019, **22**, 100119.
91 S. Zinatloo-Ajabshir, M. Baladi and M. Salavati-Niasari, *Ultrason. Sonochem.*, 2021, **72**, 105420.
92 Ch. V. Reddy, R. Koutavarapu, K. R. Reddy, N. P. Shetti, T. M. Aminabhavi and J. Shim, *J. Environ. Manage.*, 2020, **268**, 110677.
93 H. J. Khadim, A. Al-Farraji and S. H. Ammar, *Environ. Nanotechnol., Monit. Manage.*, 2022, **18**, 100722.
94 H. Chen and Y. Xu, *Appl. Surf. Sci.*, 2014, **319**, 319–323.
95 H. Fu, L. Zhang, W. Yao and Y. Zhu, *Appl. Catal., B*, 2006, **66**, 100–110.
96 Y. Zhang and Y. J. Xu, 2014.
97 R. P. Panmand, Y. A. Sethi, S. R. Kadam, M. S. Tamboli, L. K. Nikam, J. D. Ambekar, C.-J. Park and B. B. Kale, *CrystEngComm*, 2015, **17**, 107–115.
98 C. Xu, X. Wei, Y. Guo, H. Wu, Z. Ren, G. Xu, G. Shen and G. Han, *Mater. Res. Bull.*, 2009, **44**, 1635–1641.
99 F.-J. Zhang, F.-Z. Xie, J. Liu, W. Zhao and K. Zhang, *Ultrason. Sonochem.*, 2013, **20**, 209–215.
100 G. Tan, J. Huang, L. Zhang, H. Ren and A. Xia, *Ceram. Int.*, 2014, **40**, 11671–11679.
101 J. Wang, J. Li, N. Zhao, J. Sha, S. Hao, E. Liu, C. Shi, C. He and D. Wang, *Appl. Surf. Sci.*, 2015, **324**, 698–704.
102 N. D. Phu, L. H. Hoang, P. Van Hai, T. Q. Huy, X.-B. Chen and W. C. Chou, *J. Alloys Compd.*, 2020, **824**, 153914.
103 C.-J. Chang, C.-W. Wang, Y.-H. Wei and C.-Y. Chen, *Int. J. Hydrogen Energy*, 2018, **43**, 11345–11354.
104 Q. Zhao, M. Gong, W. Liu, Y. Mao, S. Le, S. Ju, F. Long, X. Liu, K. Liu and T. Jiang, *Appl. Surf. Sci.*, 2015, **332**, 138–146.
105 J. Ma, B. Zhao, X. Fan, W. Wang, X. Chen, N. Shao and P. Jiang, *Diamond Relat. Mater.*, 2022, **127**, 109143.
106 C.-J. Chang, J.-K. Chen, K.-S. Lin, Y.-H. Wei, P.-Y. Chao and C.-Y. Huang, *J. Alloys Compd.*, 2020, **813**, 152186.
107 X. Zheng, Y. Chu, B. Miao and J. Fan, *J. Alloys Compd.*, 2022, **893**, 162382.
108 J. Yang, L. Li, F. Fu, H. Xu, K. Da, S. Cao, W. Chen, L. Yang and X. Fan, *Appl. Surf. Sci.*, 2023, **610**, 155598.
109 J. Shen, J. Xue, Z. Chen, J. Ni, B. Tang, G. He and H. Chen, *J. Mater. Sci.*, 2018, **53**, 4848–4860.
110 J. Yang, X. Wang, Y. Chen, J. Dai and S. Sun, *RSC Adv.*, 2015, **5**, 9771–9782.
111 Y. Zhou, P. Lv, W. Zhang, X. Meng, H. He, X. Zeng and X. Shen, *Appl. Surf. Sci.*, 2018, **457**, 925–932.
112 B. Li, L. Tan, X. Liu, Z. Li, Z. Cui, Y. Liang, S. Zhu, X. Yang, K. W. Kwok Yeung and S. Wu, *J. Hazard. Mater.*, 2019, **380**, 120818.
113 J. Wan, Y. Zhang, R. Wang, L. Liu, E. Liu, J. Fan and F. Fu, *J. Hazard. Mater.*, 2020, **384**, 121484.

114 A. Phuruangrat, S. Buapoon, T. Bunluesak, P. Suebsom, S. Wannapop, T. Thongtem and S. Thongtem, *Solid State Sci.*, 2022, **128**, 106881.
115 X. Hu, J. Tian, Y. Xue, Y. Li and H. Cui, *ChemCatChem*, 2017, **9**, 1511–1516.
116 Z. Zhang, W. Wang, E. Gao, M. Shang and J. Xu, *J. Hazard. Mater.*, 2011, **196**, 255–262.
117 L. G. Devi, N. Kottam and S. G. Kumar, *J. Phys. Chem. C*, 2009, **113**, 15593–15601.
118 S.-S. Lee, B. T. Huy, N. T. K. Phuong, D. K. Tung and Y.-I. Lee, *Korean J. Chem. Eng.*, 2019, **36**, 1716–1723.
119 N. Tahir, M. Zahid, I. A. Bhatti and Y. Jamil, *Environ. Sci. Pollut. Res.*, 2022, **29**, 6552–6567.
120 H. Su, S. Li, L. Xu, C. Liu, R. Zhang and W. Tan, *J. Phys. Chem. Solids*, 2022, **170**, 110954.
121 C. Du, X. Ma, H. Xue, F. Wang, H. Yang, L. Zhang, L. Ma, L. Jia and K. Wang, *Bull. Mater. Sci.*, 2022, **45**, 95.
122 R. Malolan, R. S. Jayaraman, S. Adithya, J. Arun, K. P. Gopinath, P. SundarRajan, O. Nasif, W. Kim and M. Govarthanan, *Chemosphere*, 2021, **266**, 128963.
123 L. X. Lovisa, T. B. O. Nunes, R. Wilson, E. Longo, M. Daldind, M. R. D. Bomio and F. V Motta, *Dalton Trans.*, 2022, **51**, 17700–17710.
124 S. Bera, S. Samajdar, S. Pal, P. S. Das, L. A. H. Jones, H. Finch, V. R. Dhanak and S. Ghosh, *Ceram. Int.*, 2022, **48**, 35814–35824.
125 V. Koteski, J. Belošević-Čavor, V. Ivanovski, A. Umićević and D. Toprek, *Appl. Surf. Sci.*, 2020, **515**, 146036.
126 Y. Zheng, J. Bao and Y. Sun, *J. Iran. Chem. Soc.*, 2022, 1–10.
127 X. Zhong, W. T. Wu, H. N. Jie, W. Y. Tang, D. Y. Chen, T. Ruan and H. P. Bai, *RSC Adv.*, 2020, **10**, 38024.
128 X.-X. Deng, S. Tian, Z.-M. Chai, Z.-J. Bai, Y.-X. Tan, L. Chen, J.-K. Guo, S. Shen, M.-Q. Cai and C.-T. Au, *Ind. Eng. Chem. Res.*, 2020, **59**, 13528–13538.
129 M. Arif, M. Zhang, J. Yao, H. Yin, P. Li, I. Hussain and X. Liu, *J. Alloys Compd.*, 2019, **792**, 878–893.
130 M. Arif, M. Zhang, Y. Mao, Q. Bu, A. Ali, Z. Qin, T. Muhmood, Shahnoor, X. Liu, B. Zhou and S. Ming Chen, *J. Colloid Interface Sci.*, 2021, **581**, 276–291.
131 N. Mahhumane, L. M. Cele, C. Muzenda, O. V. Nkwachukwu, B. O. Orimolade, B. A. Koiki, L. Tshwenya and O. A. Arotiba, *Mater. Today Commun.*, 2022, **33**, 104804.
132 H. Luo, B. Zhao, M. Zhang, Y. Liu, R. Han and L. Liu, *New J. Chem.*, 2019, **43**, 15335–15341.
133 X. Zhang, M. Wang, X. Jia, K. Cao and M. Zhang, *ChemistrySelect*, 2019, **4**, 12785–12793.
134 R. B. Hughes-Currie, P. S. Senanayake, J.-P. R. Wells, M. F. Reid, G. Berden, R. J. Reeves and A. Meijerink, *Phys. Rev. B*, 2013, **88**, 104304.
135 R. Zamiri, A. F. Lemos, A. Reblo, H. A. Ahangar and J. M. F. Ferreira, *Ceram. Int.*, 2014, **40**, 523–529.
136 X. Wang, Z. Cao, Y. Zhang, H. Xu, S. Cao and R. Zhang, *Chem. Eng. J.*, 2020, **385**, 123782.
137 H. Wu, X. Liu, J. Wen, Y. Liu and X. Zheng, *Colloids Surf., A*, 2021, **610**, 125933.
138 N. Tian, Y. Zhang, H. Huang, Y. He and Y. Guo, *J. Phys. Chem. C*, 2014, **118**, 15640–15648.
139 H. A. Ahsaine, A. Slassi, M. Ezahri, A. Benlhachemi, B. Bakiz, F. Guinneton and J.-R. Gavarri, *RSC Adv.*, 2016, **6**, 101105–101114.
140 L. N. Guo and S. Ren, *Appl. Mech. Mater.*, 2016, **851**, 72–77.
141 H. Gu, L. Yu, J. Wang, M. Ni, T. Liu and F. Chen, *Spectrochim. Acta, Part A*, 2017, **177**, 58–62.
142 X. Zhang, M. Zhang and K. Cao, *CrystEngComm*, 2019, **21**, 6208–6218.
143 C. Wang, C. Gu, T. Zeng, Q. Zhang and X. Luo, *J. Rare Earths*, 2021, **39**, 58–66.
144 X. Li, W. Li, S. Gu, X. Liu, H. Li, C. Ren, X. Ma and H. Zhou, *J. Alloys Compd.*, 2021, **851**, 156935.
145 X. Zhang, *J. Iran. Chem. Soc.*, 2022, **19**, 3029–3041.
146 Y. Qiu, J. Lu, Y. Yan and J. Niu, *J. Hazard. Mater.*, 2022, **422**, 126920.
147 H. Li, H. Hao, S. Jin, W. Guo, X. Hu, H. Hou, G. Zhang, S. Yan, W. Gao and G. Liu, *Adv. Powder Technol.*, 2018, **29**, 1216–1221.
148 X. Li, W. Li, X. Liu, H. Fan, L. Geng, X. Ma, M. Dong and S. Liu, *J. Alloys Compd.*, 2021, **889**, 161757.
149 Z. Liu, L. Shen, X. He, E. Y. B. Pun and H. Lin, *Colloid Interface Sci. Commun.*, 2021, **44**, 100494.
150 X. Zhang, Y. Zhao, J. Li, W. Gai and Y. Gu, *J. Phys. Chem. Solids*, 2022, **171**, 110998.
151 X. Li, W. Li, X. Liu, L. Geng, H. Fan, X. Ma, M. Dong and H. Qiu, *Appl. Surf. Sci.*, 2022, **592**, 153311.
152 M. Shang, W. Wang, L. Zhang and H. Xu, *Mater. Chem. Phys.*, 2010, **120**, 155–159.
153 H. A. Ahsaine, *Etude de tungstate de bismuth (Bi, Lu) 2WO6: Evolution des propriétés physicochimiques, luminescentes et photocatalytiques*, PhD thesis, Ibn Zohr, 2016.
154 X. Ding, K. Zhao and L. Zhang, *Environ. Sci. Technol.*, 2014, **48**, 5823–5831.
155 H. Huang, K. Liu, K. Chen, Y. Zhang, Y. Zhang and S. Wang, *J. Phys. Chem. C*, 2014, **118**, 14379–14387.
156 Y. Fu, C. Chang, P. Chen, X. Chu and L. Zhu, *J. Hazard. Mater.*, 2013, **254**, 185–192.
157 L. H. Hoang, N. D. Phu, H. Peng and X.-B. Chen, *J. Alloys Compd.*, 2018, **744**, 228–233.
158 Y. Zhang, Y. Zhao, Z. Xiong, T. Gao, B. Gong, P. Liu, J. Liu and J. Zhang, *Appl. Catal., B*, 2021, **282**, 119534.
159 Y. W. Teh, C. Er, X. Y. Kong, B. Ng, S. Yong and S. Chai, *ChemSusChem*, 2022, **15**, e202200471.